

Paving the Way for Large Scale Arrays of Photonic THz Transmitters



Adam Alderton

Centre for Doctoral Training - MRes in Connected Electronic and Photonic Systems
2021 - 2022

Registered student at the University of Cambridge
Supervised by Prof. Cyril Renaud

I hereby declare that the work submitted herein is my own original work.
Signed: Adam Alderton. Date: June 4, 2022.

Abstract

A key challenge that remains in the field of sub-THz is the fabrication of a high power, steerable source for use in short-to-medium range machine-to-machine communications operating at 300 GHz [1]. A roadblock in the realisation of such a device is the ‘terahertz gap’: the immaturity of technologies for the generation and detection of THz light [2]. A well-understood workaround for this issue is the process of photomixing two laser beams with a uni-travelling carrier photodiode (UTC-PD) which can then produce high power photocurrent at sub-THz frequencies. This photocurrent can be used to drive emission from an antenna at these desired sub-THz frequencies [3]. An obstacle that is largely unaddressed within this wider goal concerns investigating how to effectively couple the laser beams into the UTC-PD for high-power generation. When a dual-mode vertical cavity surface-emitting laser is used to generate the two beams used for photomixing, a lensing structure is required to counter the natural divergence of these beams such that they converge onto the UTC-PD. This lensing structure should focus the beams accurately, perform at high power transmissivity and, importantly, be compatible with mature fabrication techniques such that such a steerable source could be realised commercially. This work proposes a fully parameterised and theoretically understood workflow of a metalens to address this challenge. For nominal yet reasonable parameters with which this design workflow is parameterised in this work, the designed lens, when numerically simulated, displays a power transmissivity of around 90% across a 300 GHz band centred around 193.4 THz. Additionally, the simulated lens possesses a focal length $0.5 \mu\text{m}$ (0.49%) away from the intended design value. Future work is needed to fully validate these results with a full simulation. The metalens design is justified to be well-matched with widely employed fabrication techniques that may be optimised using the planar design of the metalens.

Contents

1	Introduction	3
2	The Subsystem	4
2.1	Devices, Materials and Dimensions	6
2.2	Theory	7
2.3	Lens Design Considerations	11
2.4	Metalens Design	15
2.5	Preliminary Fabrication Discussion	16
2.6	Subsystem Outline and Summary	17
3	Mapping Required Phase to Metasurface Elements	20
4	Lens Design Evaluation	25
4.1	Focusing Accuracy Further Discussion	30
4.2	Power Coupled	31
4.3	Lens Evaluation Summary	34
5	Future Work	34
6	Conclusion	35

1 Introduction

Machine-to-machine (M2M) connections will be half of the global connected devices and connections by 2023 by which there will be 14.7 billion M2M connections [4]. Of these, connected home applications will have the largest share at 48%, closely followed by connected personal vehicles with 30% [4]. The large yet still increasing demand for connected devices necessitates demand for high data rate, wireless communications. The ultra-high frequency of the sub-THz band, around 300 GHz, is fast becoming a promising candidate to meet this demand as evidenced by the official specification of the lower THz frequency range for wireless, high data rate applications [5, 6]. It also promises to be compatible with short-to-mid range communications as there is a 120 GHz wide band of low-loss atmospheric propagation limited by two spikes in water absorption attenuation [1]. This band comes close to enabling tera-bit s^{-1} data rates such that the speeds of wired and wireless communications are expected to converge in the coming years [4, 6]. An additional benefit of the wireless approach is the decrease in latency due to the increased propagation of light in air as opposed to optical fibre due to the lower dielectric constant rendering the wireless approach superior for real-time, high data rate applications [1, 7].

A common practice for sub-THz communication and other wireless communication is to employ a technique known as beam steering [7, 8]. This is the practice of modulating the emission phase of a phased array of antennas such that the cumulative wavefront produced is highly directional [7]. In that sense, if it is known where the power of the beam is needed to be received then the relative phases of the emission of the antennas in the array can be optimised to emit as much power as possible in the direction it is needed. Additionally, the use of a collection of antennas in a phased array yields a higher collective power than a single antenna alone.

A current challenge in the field of sub-THz communications is the need for a high power steerable source [1]. This is the challenge that this project begins to address. The reason this niche remains largely unfilled is due to the *terahertz gap* - a range of frequencies on the order of 0.1 to 10 THz in which pragmatic technologies for radiation emission and detection are incredibly limited [2]. This of course includes 300 GHz. To address this, a well-established ‘workaround’ is often employed: photomixing [1, 2]. Photomixing here is the process of setting two beams of slightly differing frequencies toward a photodetector such that the photodetector is sensitive to the beat note of the interfering frequencies thus yielding a photocurrent in the photodetector with a frequency equal to that of the difference in frequencies of the initial beams [7, 9]. The photocurrent generated may then be used to drive an antenna which will operate at a matching frequency. In the context of the generation of sub-THz radiation, two coherent THz beams may be photomixed.

To put the photomixing process into practice, a dual-mode vertical cavity surface-emitting laser (DM-VCSEL) can be coupled to a uni-travelling carrier photodiode (UTC-PD) for sub-THz photomixing, the details of which are to be discussed in Section 2 [10]. In this system, however, the DM-VCSEL beam diverges significantly such that the area swept out by the beam is significantly larger than the active area of the UTC-PD. Therefore, intuitively, only a small fraction of the power

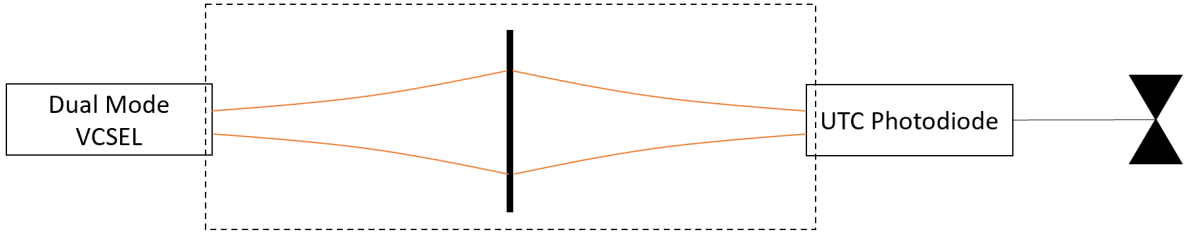


Figure 1: An abstracted view of the subsystem that is the focus of this work. Particularly, the area inside the dashed rectangle. That is, the emergence of a Gaussian beam from a dual-mode VCSEL and its convergence onto a UTC-PD via a thin lens. The photocurrent generated from the photomixing of the dual laser modes in the UTC-PD is used to drive an antenna represented by the bow-tie shape on the far right of the figure. More details about this subsystem are given in Section 1 and in Section 2.

transferred in the DM-VCSEL beam is incident on the UTC-PD.

The work presented here addresses this issue by incorporating the design of a lensing structure to focus the otherwise diverging DM-VCSEL beam onto the UTC-PD. An abstract summary of this system is shown in Figure 1. The antenna array used to perform beam steering is depicted in Figure 2. In particular, this project aimed to produce a design framework for a lensing structure for use in this subsystem that provides high power coupling and is practical for fabrication and packaging as part of a wider device. To this end, the project yielded a design flow for a metalens and tested a design based on nominal yet realistic parameters. Within this, theoretical principles of the subsystems were first established which was followed by a discussion of the various devices, parameters and lens types available all in the interest of coupling ability and practicality. With the theoretical description and the practical details finalised, the lens design workflow was put together. With this, a metalens was designed with the nominal parameters and was evaluated to measure its performance in the context of the DM-VCSEL, UTC-PD coupling subsystem.

To carry out the design framework and evaluate the design, an electromagnetic simulation software called CST studio suite was used. This software numerically evaluates Maxwell's equations for a meshed structure with either time domain or frequency domain solvers - both of which have their advantages [11]. Additionally, the software facilitates the use of GPU and memory accelerated computing with an associated GPU cluster which was crucial for the evaluation of the complex structures used throughout this project.

2 The Subsystem

Here introduced is the photomixing subsystem in more detail. An initial introduction to the subsystem is given in Section 1.

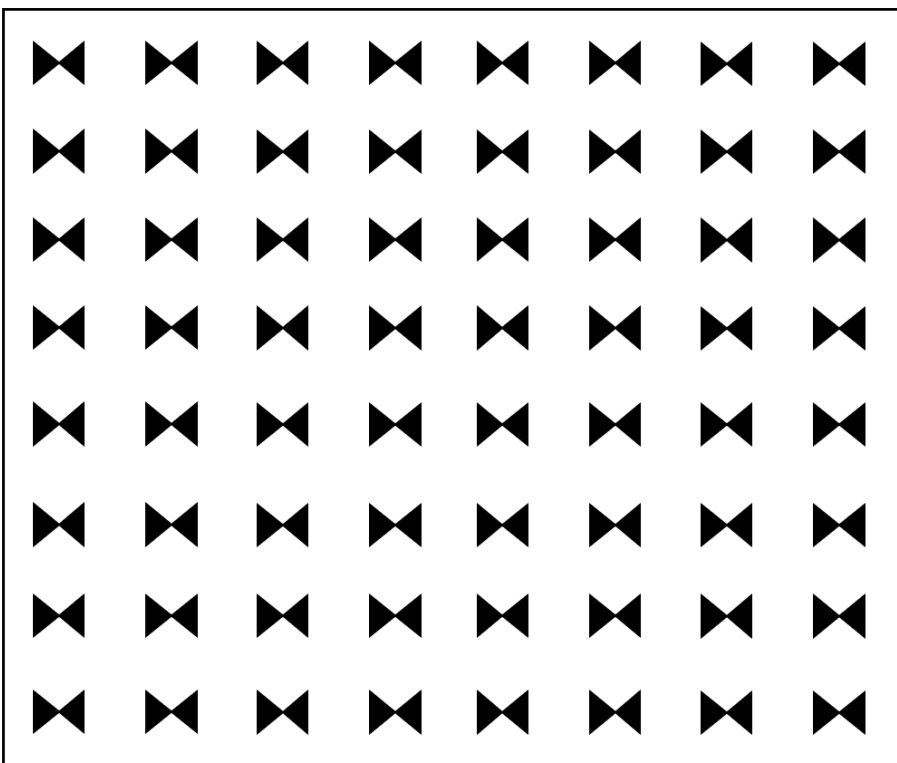


Figure 2: A simple graphical view of what a phased antenna array used for beam steering may resemble. Each bow-tie antenna is driven by a DM-VCSEL, UTC-PD photomixing subsystem matching the one displayed in Figure 1. Here, an 8×8 antenna array is shown.

2.1 Devices, Materials and Dimensions

First, we consider the DM-VCSEL and the general motivation behind the use of photomixing in this context. An important discussion to have is that of the alternatives to the DM-VCSEL for this approach. Cutting-edge electronic sources operating at 300 GHz are not suitable for the antenna array discussed here due to their large form factor [12]. Secondly, direct photonic sources operating with high power at 300 GHz are currently impractical due to the previously mentioned terahertz gap, thus the photomixing approach [2]. It should also be noted that there are significant challenges with photomixing two separate beams generated from two separate single-mode lasers. In particular, it is challenging to efficiently merge the initially separate beams on-chip[1]. With the DM-VCSEL, UTC-PD photomixing approach recognised, it is necessary to benchmark the current performances of this approach. Good progress has been made in creating a DM-VCSEL, UTC-PD photomixing system however previous work has struggled to achieve high power with low-loss, mass-producible monolithic integration [1, 13, 14, 15]. Of course, the total power output of the beam steered THz array depends on the number of ‘unit cell’ antennas and the power emitted by each unit cell. Therefore, if higher power DM-VCSEL sources can be engineered instead of the naive addition of more antennas, then a more compact collective device can be produced for high power throughput [16].

We next discuss the motivation behind the use of the UTC-PD. The use of the UTC-PD for THz photomixing is well understood and has been successfully implemented numerous times [3, 10, 17]. The reasoning behind the use of the UTC-PD in this work and previous is due to its unique ability to operate at higher speeds with higher output in the sub-THz range when in direct comparison with other common devices such as p-i-n photodiodes [18]. This is due to the typical design of the device which ensures that only electrons operate as charge carriers in the device [18]. Electrons in the structure display a much lower effective mass, hence higher mobility which can lead to them travelling at near ballistic velocities [10, 19].

With the DM-VCSEL, UTC-PD photomixing system established, it is important to discuss the structural parameters of a monolithic device that would house them. Remembering that the DM-VCSEL, UTC-PD, antenna subsystem is a unit cell in a wider phased array device, we can discuss the properties of the unit cell. The unit cell should tessellate therefore a square unit cell is a natural choice for its simplicity [8].

A first design constraint for the square unit cell is that it needs to house an antenna. With the nominal yet informed choice of a typical bowtie antenna operating in the sub-THz band [20], we can opt for the surface area of the unit cell to be $250 \mu\text{m} \times 250 \mu\text{m}$.

An important consideration is the distance between the DM-VCSEL and the UTC-PD. High power coupled would of course be achieved if the devices were brought close together, perhaps on the order of a few micrometres, however brittleness of the incredibly thin device would render it impractical. Therefore, the nominal choice for the length of the unit cell structure is $800 \mu\text{m}$ with the lensing structure lying halfway at $400 \mu\text{m}$. There is a trade-off to be had with the length of the unit cell due to an interaction with the lensing structure - this is discussed in detail in Section 2.3.

Finally, we consider the materials with which the subsystem should be fabricated. Here, we only consider the materials from which the lensing structure and the bulk of the 800 μm long unit cell. The materials used in DM-VCSEL and UTC-PD should be tailored with consideration of the wider system as part of the future work on the project. During the early stages of the project, several materials and material classes were considered. The materials considered should aim to provide three main benefits: structural integrity, ease of manufacture and ideally a high permittivity constant such that THz electromagnetic radiation generated by the antenna on top of the structure is encouraged away from the structure and to propagate outwards. To meet these needs, polymers were first considered. Polymers in this context can be generalised to be very easy to deposit in mass however they tend to have lower permittivities than alternatives and adhesion to external metal patterning is challenging [21].

Silicon oxide (silica) in conjunction with another linked patterning material, including silicon nitride or amorphous silicon, is a material used commonly in the field of integrated optics to exert refractive index profiles to build structures such as graded-index (GRIN) lenses [22]. Crucially, crystalline fused silica is index-matched with its glassy form ensuring simple integration with the use of bulk glass in the manufacturing process [11]. A glassy silicon oxide substrate also demonstrates strong structural properties [11].

With the various common material selections for similar purposes examined, a silica substrate was selected to constitute the bulk of the subsystem with an amorphous silicon structure to build the lensing structure, to be detailed in Section 2.3.

2.2 Theory

Before a lensing structure can be decided upon, a theoretical groundwork must be laid such that a fully informed decision can be made as to what design of lens may operate most effectively in the system.

A common approximation used in the analysis of simple lensing systems is that the lens is considered to be *thin* meaning that the light it interacts with can be assumed to experience no spatial transformation effects [7]. Simply, the lens is physically thin with respect to the dimensions of the wider system. With this approximation, it can be understood that a thin lens, due to exerting an optical path difference, is a simple phase transformation of the form [23]

$$\phi(\rho) = \frac{k\rho}{2f} \quad (1)$$

where k is the wavenumber of a beam in the surrounding material, f is the focal length of the lens and ρ is the radial distance of a point from the optic axis (centre) of the lens. In Cartesian space where the thin lens lies in the $x - y$ plane, $\rho = \sqrt{x^2 + y^2}$. It must be noted that this phase transformation assumes that the beam in question conforms to the paraxial approximation where it propagates along the positive z axis [23]. With these assumptions in place, we can state that a complex wavefront U_A

situated just before a thin lens will be transformed to a complex wavefront U_B just after the lens by the operation of the phase profile on the initial wavefront U_A :

$$U_B = \exp\left(\frac{k\rho}{2f}\right) U_A. \quad (2)$$

Therefore, importantly, the focal length of the lens fully parameterises the transformation of U_A to U_B . That is, if U_A and U_B are known then f can be derived and if U_A and f are known then U_B can be derived.

Next, we process a more rigorous understanding of the emitted DM-VCSEL beam. For this project, we will assume that the VCSEL is emitting within its fundamental TEM₀₀ mode which is in strong agreement with a spherical Gaussian beam [24]. This assumption is challenged later in Section 5.

Gaussian beam propagation and diffraction in isotropic, non-linear media is well understood [11, 24, 25, 26]. The complex amplitude of a Gaussian beam propagating parallel to the positive z direction is [11]

$$U(\mathbf{r}) = A_0 \frac{W_0}{W(z)} \exp\left(-\frac{\rho^2}{W^2(z)}\right) \exp\left(-jkz - j\frac{k\rho^2}{2R(z)} + j\xi(z)\right) \quad (3)$$

where ρ is the radial distance of a point from the optical axis as with equation (1), A_0 is an amplitude with the units of the complex quantity under representation which in this case is the electric field [11]. Continuing, W_0 is the half-width of the minimum *waist* of the beam; a characteristic width of the beam when the beam width is smallest - it is focused [24]. The waist is conventionally defined to be the width at which the (complex) amplitude of the beam falls to $1/e^2$ of its maximum value [11]. Similarly, $W(z)$ tracks the waist of the beam at it propagates along z and is defined as [11]

$$W(z) = W_0 \sqrt{1 + \left(\frac{z}{z_0}\right)^2} \quad (4)$$

where z_0 is a characteristic length of the beam called the Rayleigh length. The quantity z_0 is a measure of the divergence of the beam: it is the length at which the waist of the beam increases by $\sqrt{2}$. That is, $W(z_0) = \sqrt{2}W_0$. Another parameter of the Gaussian beam described by equation (3) is $R(z)$ which is the radius of curvature of the beam, which of course changes as it propagates [11]. It is defined by

$$R(z) = z \left[1 + \left(\frac{z_0}{z} \right)^2 \right]. \quad (5)$$

A quantity to briefly discuss the quantity $\xi(z)$ which is known as the Gouy phase: a change in phase of a Gaussian beam associated with it passing through its focus [11]. Assuming the focus lies at $z = 0$ [11],

$$\xi(z) = \tan^{-1} \left(\frac{z}{z_0} \right). \quad (6)$$

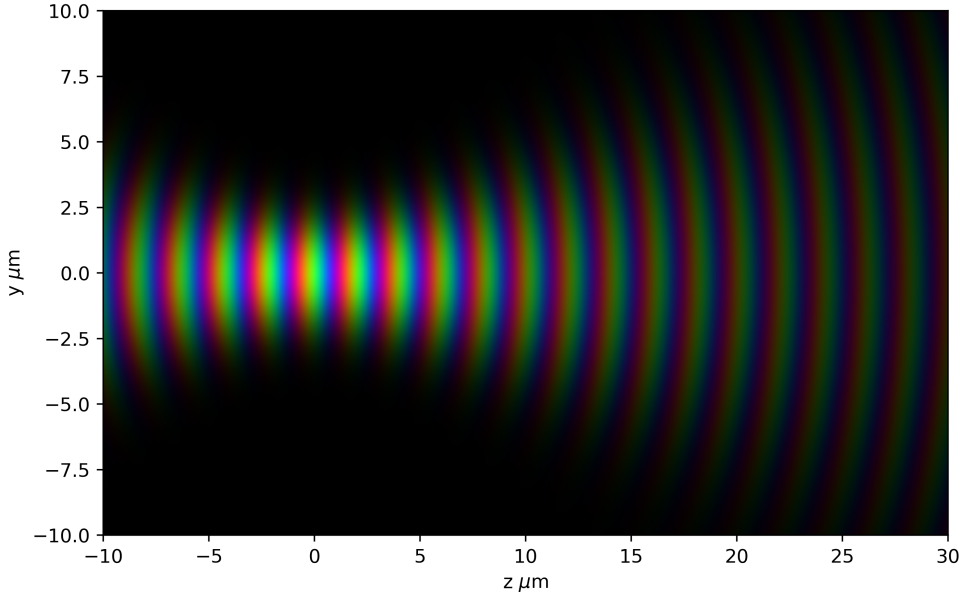


Figure 3: The complex electric field of an arbitrary Gaussian beam generated with the use of equation (3) propagating in the positive z direction, evaluated along the $x = 0$ plane. The amplitude of the field is represented by colour brightness while the phase is represented by the colour itself. The beam has an initial waist $W(0) = W_0 = 2 \mu\text{m}$, a wavelength $\lambda = 2 \mu\text{m}$ and therefore a Rayleigh length $z_0 = 6.28 \mu\text{m}$ by equation (7). The convergence and subsequent divergence of a Gaussian beam around its focus can be seen.

Lastly, it must be noted that W_0 and z_0 are intimately linked [11]:

$$W_0 = \sqrt{\frac{\lambda z_0}{\pi}}. \quad (7)$$

Using equation (7), a Gaussian beam can be fully described using any two of the three parameters W_0 , z_0 and λ . Typically, z_0 and λ are used especially as λ is a function of the material in which the beam is propagating through: $\lambda = \lambda_0/n$ where n is the refractive index and λ_0 is the free-space wavelength.

A Gaussian beam propagating into and out of its focus is shown in Figure 3. A schematic of a general Gaussian beam is given in Figure 4.

With the theory for the propagation of the Gaussian beam investigated, it is important to understand how the theory links to the subsystem this work is aiming to design and simulate. Discussion early in this section noted that the thin lens phase profile is subject to the assumption that the wavefront it operates upon conforms well to the paraxial approximation. However, Gaussian beam wavefronts are only flat ($|R| = \infty$) at three, mostly unhelpful, points: $z = 0, z = \pm\infty$. This can be found on inspection of equation (5). More importantly, by differentiating $R(z)$ with respect to z we find that the radius of curvature of a Gaussian beam is minimal at $z = z_0$. That is, the wavefronts are ‘least flat’ or ‘most curved’ at $z = z_0$ and hence most break the paraxial approximation at this plane.

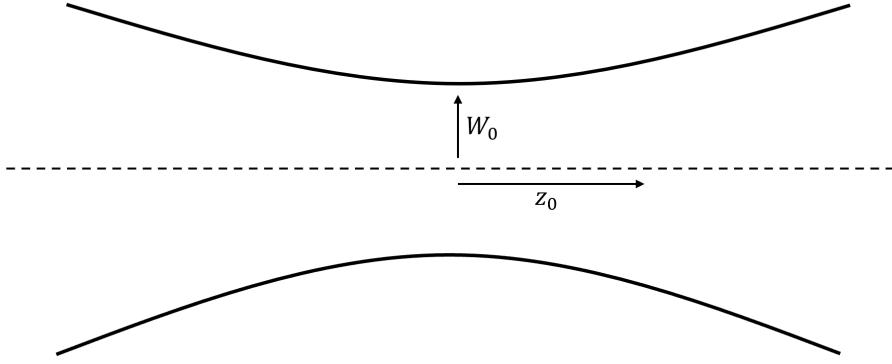


Figure 4: A graphical schematic of a general Gaussian beam about its focus as it propagates from the left side of the figure to the right. The solid lines represent the waist of the beam and the dashed line represents the optical axis: the centre of the beam. Shown is the initial waist W_0 and the Rayleigh length z_0 .

This is an issue to be factored in when designing the subsystem. This approximation limitation will be brought together with the physical implementation in Section 2.6.

With the Gaussian beam propagation understood, we now derive an analytical link between the subsystem parameters, subsystem device parameters and the lens focal length f which fully describes its phase exertion. We do this by evaluating equation (1). As the lens is thin, the equation reduces to relating the phases of the beam just before and just after the lens [11]:

$$kz + \frac{k\rho^2}{2R} - \xi - \frac{k\rho^2}{2f} = kz + \frac{k\rho^2}{2R'} - \xi \quad (8)$$

where R is the radius of curvature of the initial beam U_A the lens and R' is the radius of curvature of the beam after the lens, evaluated at the lens [11]. This then reduces to

$$\frac{1}{f} = \frac{1}{R} - \frac{1}{R'}. \quad (9)$$

Therefore, we have a relation between the beam properties before and after the lens and the focal length of the lens itself. R can be evaluated from the DM-VCSEL properties and unit cell size parameters using equations (7) and (5). Similarly, R' can be evaluated by considering where the UTC-PD is and how far the beam is to propagate to it. Importantly, this equation accounts for the varying phase across the wavefront at the lens due to the curvature of the wavefront. An abstracted depiction of the subsystem to understand this relationship is given in Figure 11. Parameterising equation (9) with known system parameters, we find that

$$\frac{1}{f} = \left(z_A + \frac{\pi^2 W_{0,A}^4}{\lambda^2 z_A} \right)^{-1} + \left(z_B + \frac{\pi^2 W_{0,B}^4}{\lambda^2 z_B} \right)^{-1} \quad (10)$$

where z_A is the distance between the beam waist of the Gaussian beam emitted by the DM-VCSEL (assumed to be at the aperture of the DM-VCSEL) to the thin lens, z_B is the distance from the thin lens to the UTC-PD, $W_{0,A}$ is the initial waist of the initial Gaussian beam and $W_{0,B}$ is the waist of the focused Gaussian beam once it travels a further z_B beyond the lens to reach the UTC-PD. It should be noted that the minus sign apparent in equation (9) is no longer apparent in equation (10) as the radius of curvature symmetry $R(-z) = -R(z)$ was used to evaluate the negative radius of curvature associated with extrapolating the beam backwards from the UTC-PD toward the lens.

A final quantity of interest to discuss as part of the theory is the *depth of focus* of the Gaussian beam. This is a measure of the distance at which the Gaussian beam stays approximately ‘focused’ [11]. This is linked to the fact that beams with smaller W_0 diverge more (smaller z_0) for constant λ , while analogously beams with larger W_0 diverge less. The depth of focus is equal to twice the Rayleigh length and is defined such that it is centred on the plane where W_0 is, typically $z = 0$ [11]. Therefore, a Gaussian beam can be justified to be ‘very nearly focused’ at a z plane if that plane lies within the depth of focus.

2.3 Lens Design Considerations

Two dominant paradigms for lens design exist: *refractive* lenses and *diffractive* lenses [7, 27]. Diffractive lenses operate in the regime of wave optics whereas refractive lenses operate under the approximations of beam optics [28]. More precisely, diffractive lenses have feature sizes of the order of the wavelength of the light hence they are able of exerting bespoke phase profiles [28]. The simplest and often most powerful phase profile aims to simply focus the light on a particular point, although this can be out of the shadow of the lens due to the capabilities of diffractive optics [27]. Finally, diffractive lenses applied to THz radiation are often less cumbersome than their refractive counterparts due to the inflexibility of the design of refractive lenses [28].

Before the discussion on the viability of various diffractive lens types for use in this subsystem can take place, the desired properties of the lensing structure must first be outlined. Most importantly, the lens must be capable of exerting the correct phase profile, ideally in a continuous manner, such that the initial Gaussian laser beam is focused onto the UTC-PD such that a maximal amount of power is coupled. Secondly, the lens must be large enough such that it apertures a vast majority of the diverging beam so that the vast majority of the beam power is focused. Next, the lens should operate with very small absorption losses and display a very high transmission coefficient. That is, it reflects very little of the beam. While these properties are desired of almost all lenses, there are a few that are specific to this project. Most importantly, the lens design must be simple and cost-effective to manufacture en masse. As to be discussed further in Section 2.5, the lens design should be near planar to allow for seamless monolithic integration with the bulk, planar surfaced substrates on either side of the lens.

Three common lens types that are often used to meet the majority of these requirements are Fresnel lenses, GRIN lenses and metlenses. A review of each of these and their viability follows.

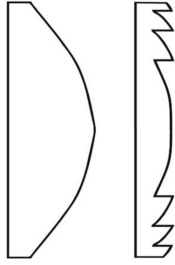


Figure 5: A classical refractive lens (left) and a refractive Fresnel lens (right), both of which display the same radius of curvature of the curved faces [28].

A very common and well-understood approach for focussing THz waves with diffractive optics is the use of a Fresnel lens [28, 29]. Fresnel lenses lie somewhere between the definitions of diffractive optics and refractive optics, depending on their application. Their macroscopic usage in lighthouses for example operates via refraction in which only the air-lens boundaries are important, as is the case for all refractive lenses in air [7]. In short, refractive Fresnel lenses operate by conserving the curvature of a classical lens but flattening the overall profile, as shown in Figure 5. The same design principle can be extended to diffractive lenses by considering the optical path difference than can be exerted by differing thickness areas of the lens [29].

With known substrate and lens refractive indices and a phase profile that needs to be exerted, Fresnel lenses can be easily designed as shown in Figure 6. The technology to manufacture such structures with continuously varying surfaces is not yet established, hence Fresnel lenses on the length scales associated with this work need to be ‘stepped’, as shown in Figure 6 [27, 28]. This can be achieved by using a series of lithographic masks such that, if engineered correctly, each can double the etching precision to tend closer to a smooth surfaced Fresnel lens, as also outlined in Figure 6 [29].

However, this geometrical complexity can render them challenging to produce at the wafer scale, especially at high throughput [30]. Additionally, in this context, a Fresnel lens design would struggle to adhere to the thin lens approximation. This is due to a necessary trade-off between material reflectivity and optical path length exertion. That is, high refractive index materials allow for more optical path exertion over a smaller distance (closer to thin lens approximation), however, exhibit high reflectivities due to a larger difference in refractive index with respect to the substrate [7], and *vice versa*. Therefore, it would be worthwhile to consider lens designs where this trade-off can be circumvented such as the use of a metasurface, as examined later in this section.

Another type of lens considered for this project is a GRIN lens. GRIN lenses have been used extensively to focus THz Gaussian beams, fabricated by various means [31, 32, 33, 34]. This lens methodology is diffractive on the length scales appropriate to this work [32]. Techniques used to manufacture these types of lenses include 3D printing and the stack-and-draw technique, both of which are capable of producing planar GRIN lenses [32, 33]. However, the speed of 3D printing inherently limits its high throughput manufacturing capabilities [33]. The stack-and-draw technique

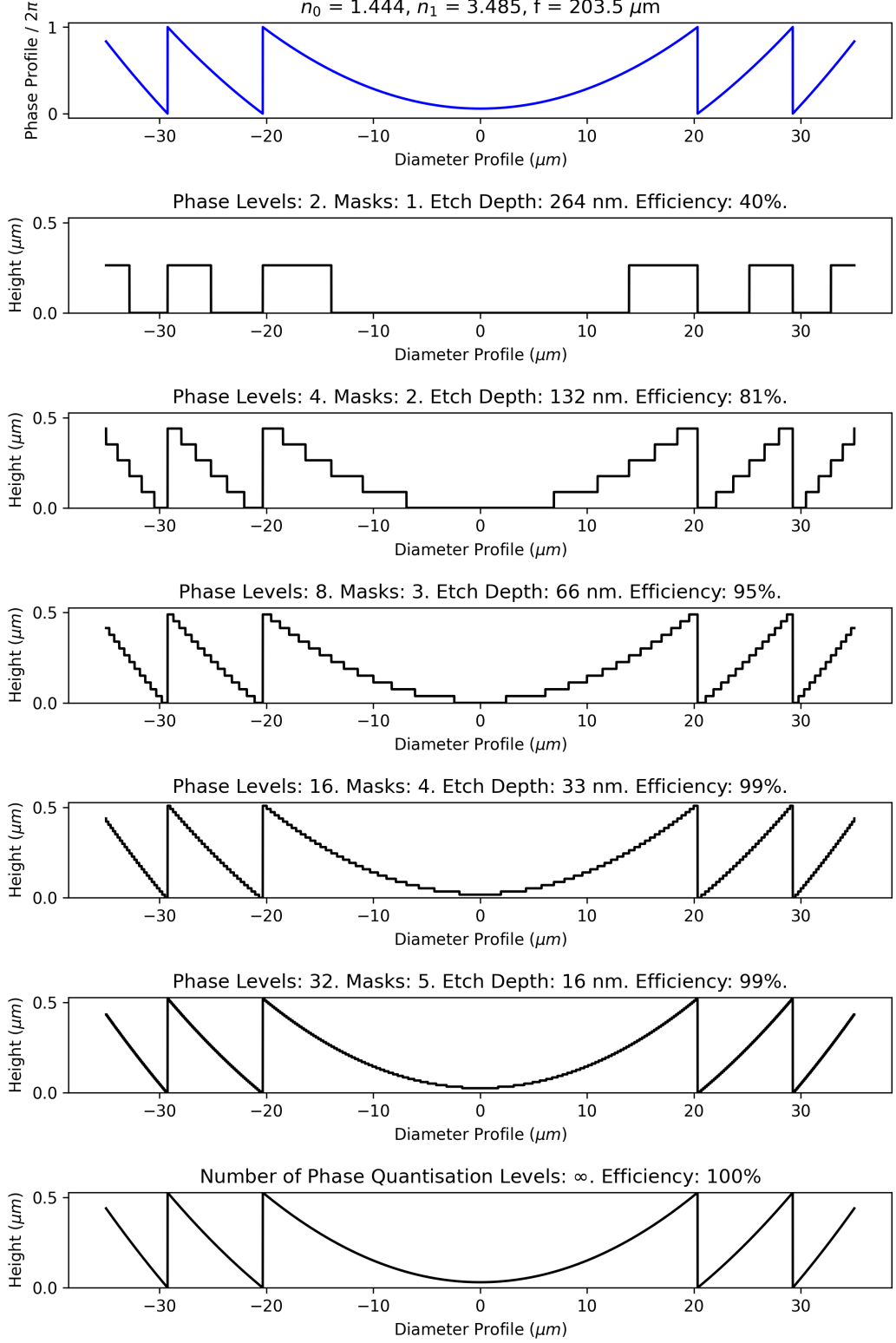


Figure 6: Various Fresnel lens profiles designed to exert the phase profile given in the top-most figure, shown in blue. The phase profile matches that given in Section 2.6. As each Fresnel lens is addressed moving down the page, one extra lithographic mask is used for its manufacture [29]. For each Fresnel lens given, its number of phase levels, number of phase masks, the etching depth required with the last mask and its diffraction efficiency are given, following the literature for theoretical efficiency [29]. The Fresnel lenses are assumed to consist of amorphous silicon and are suspended in silica surroundings as outlined in Section 2.1. These Fresnel lenses are shown to emphasise their complexity cost for high diffraction efficiency.

is capable of large batch manufacture of these lenses, but further adhesion and integration with the subsystem are needed: the lenses are not produced directly on the substrate [32]. GRIN lenses can also be produced by inducing a dopant gradient in a material, a common combination in Ge doped Si [35]. This approach produces long cylindrical lenses which are incompatible with the thin lens approximation assumed here [35]. Additionally, the high rate of manufacture of these lenses and their subsequent integration in the wider subsystem would be challenging as each lens must be carefully epitaxially grown and aligned with the DM-VCSEL and UTC-PD. Gaussian beam propagation through a ‘non-thin’ GRIN lens is theoretically understood but it is significantly more complex than our thin lens system proposed here [34]. Therefore, for manufacturing and theoretical complexities, GRIN lenses in this context are likely not the optimal choice for the lensing structure.

Finally, we discuss the *metалens* approach, which is the approach that is adopted in this work. First, some disambiguation is required. The term ‘metalens’ can loosely be applied to any lens structure with any features with sizes less than the wavelength of light they are intended to function at [7]. For example, some of the diffractive Fresnel lenses and diffractive GRIN lenses discussed earlier in this section can be labelled as metalenses except that they follow a specific design principle. Indeed, many metalens design paradigms don’t conform to any classical lens design approach, such as the plasmonic metalens [30].

The details of the specific metalens design methodology used are given in Section 2.4, however general metalens properties and advantages are discussed here. Metalenses, like all lenses that operate via diffractive optics, aim to exert a specifically designed phase profile onto a wavefront [36]. The means by which this is achieved varies [36]. As a simple example, the diffractive Fresnel lens approach exerts a phase profile by controlling optical path difference by varying the length of the higher-index material that the beam must pass through [27]. However, the GRIN lens design applies a phase profile by varying the index of the material for constant thickness [34]. Many metalens designs, such as the one implemented here, operate on a variable scattering principle [30]. That is, structures such as nano-rods are placed across a surface to scatter the incident radiation in slightly different ways such that the collective behaviour is that of a lens [30].

For practical purposes within this project, a metalens approach has three distinct advantages and one potential disadvantage. The first of which is that metalenses have been shown to have superior transmission and focussing properties when compared to other diffractive optical elements such as Fresnel lenses [37]. This allows for greater flexibility in the system parameters as it is less likely that the limitations of the lens will be a factor. The second advantage is that they can be designed to greatly fulfil the thin lens approximation by the use of sub-wavelength length nano-rods, for example [30]. The final and most important advantage is that they can be easily manufactured to be planar using CMOS compatible fabrication techniques [36]. That is, high capacity monolithic fabrication and integration are possible which is pertinent to the practical and commercial viability of the product of this work. The potential disadvantage of the metalens approach is that they are known to suffer greatly from dispersive effects [36]. That is, their effective bandwidth is small. However, as to be considered in Section 2.6, these dispersive effects should be minimal as the difference in frequency of

the beams used for photomixing (approximately 300 GHz) is less than 1% of the nominal emission wavelength from the DM-VCSEL.

In summary, following the discussion of classical diffractive optical elements and metalenses, the metalens approach can be sensibly deemed to be a strong concept to move forward with.

2.4 Metalens Design

With a metalens design justified to be the lensing structure in the subsystem, the focus must now be turned to the details of the design. Following work on plasmonic metalenses operating in the THz region in conjunction with the discussion on materials given in Section 2.1, an amorphous silicon cylindrical nano-rod metasurface on a glass/silica substrate was settled upon [30, 37]. The nano-rods are organised in a square lattice on the substrate with a sub-wavelength lattice constant.

This metalens design can be understood to function as follows. Each nano-rod has a well-defined length and diameter. The phase exerted on an incident beam by a rod is a function of its length and its diameter, as to be discussed in Section 3. Therefore, with the necessary phase needed at a particular lattice point known, a nano-rod with an appropriate length and diameter can be constructed at that lattice point to provide that particular phase shift. For ease of manufacture, the length of the nano-rods can be fixed such that only the diameter of the rods needs to be controlled across the lens profile. However, it is important to initially choose a constant rod length such that a full phase modulation between 0 and 2π can be achieved, which is often challenging in diffractive optics [28]. It is possible to choose a nano-rod height to achieve this full phase exertion with high transmission as shown in Section 3 and previous work in the field [30].

How exactly the nano-rods exert a phase shift on an incident beam can be recognised as follows. It can be shown that nano-rods such as this approximate the behaviour of isolated, non-interacting scatterers [30]. That is, there is very little coupling between adjacent nano-rods and even less coupling between non-adjacent rods, and even less again between non-local rods [30]. It has been shown that light is concentrated inside the rods and as such the rods operate analogously to weakly-coupled, low Q-factor resonators [30]. It is this concentration of light inside the rods that allows each rod to independently exert its phase exertion to its portion of the beam [30].

Following the nominal yet informed 2D phase profile needed which is introduced in Section 2.6, the following lens was produced. The lens has a radius of 35 μm and consists of 6006 a-Si nano-rods of height 1150 nm the diameters varying between 100 nm and 504 nm, all organised on a square lattice with a lattice constant of 800 nm. The structure is displayed in Figure 7.

Before the discussion on the design of the lens can conclude, an important design trade-off needs to be addressed. The trade-off is a three-way dependency between the beam properties at the lens, the number of rods and the capacity to simulate the system. Importantly, the beam to be focused needs to experience a near-continuous phase profile across the lens such that the collective (but not coupled) scattering of the rods closely matches the behaviour of a classical lens. Therefore, for a constant lattice constant, the beam area needs to increase such that it ‘experiences’ more rods. To

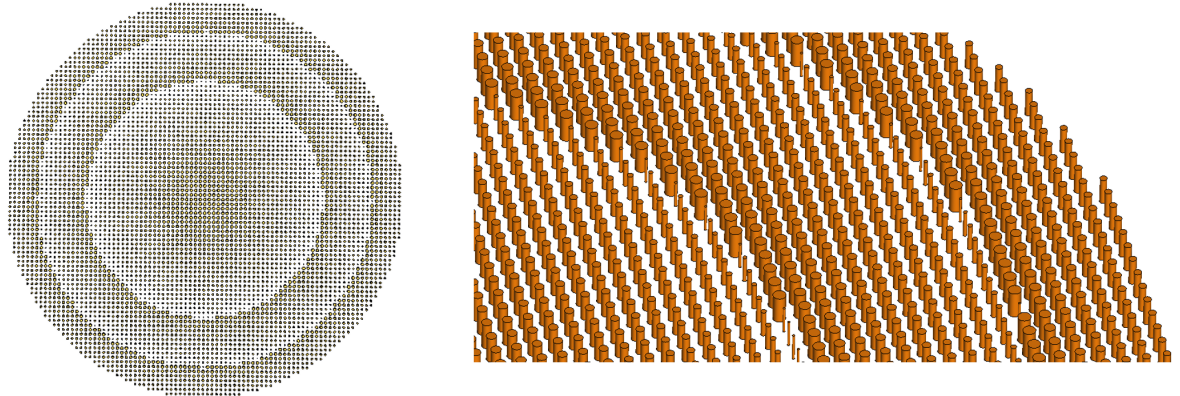


Figure 7: The lens produced following the design workflow given in Section 2.4 provided with the parameters given in Section 2.6. (left): The full lens. (Right): A portion of the lens viewed closely and angled slightly. A clear diagram of the lens structure with length measurements is given in Figure 10.

achieve this, the Gaussian beam emitted, which has an initial waist of the order of five micrometres, needs to be allowed to propagate far enough such that it sufficiently diverges. This links back to a previous discussion in Section 2.2 regarding issues around the radius of curvature of the beam, especially in the region of the Rayleigh length z_0 . Therefore, combining these, the beam needs to be allowed to propagate far enough such that it is sufficiently beyond z_0 before it reaches the lens *and* far enough such that the discrete nature of the rods tends to a continuum.

Therefore, ideally, the beam would be allowed to propagate much further than both of these points, even if the rod continuity point is ill-defined. However, there are three important constraints on how far we can allow the beam to propagate. Firstly, any substrate material absorption losses are increased by propagation distance. Secondly, a larger lens to accommodate for a larger divergence would require much more manufacturing power as the number of rods is proportional to the area of the lens, which is proportional to the radius of the lens by πr^2 . In short, a slightly larger lens requires many more rods. Thirdly and most importantly, the many more rods required by a larger lens require much higher compute and memory overheads to simulate. Even with the GPU cluster available to carry out this work, only a number of rods on the order of 1000s of rods can be simulated. However, empirically, it is unlikely that the use of 1000s of rods breaks the rod-continuum approximation. To summarise the most pertinent points of this trade-off, the number of rods needs to be large to uphold beam curvature and size approximations but the number of rods is limited by the computing power available to the simulation software.

2.5 Preliminary Fabrication Discussion

While the specifics of the fabrication of the lens, the wider subsystem and the wider system are mostly out of the scope of this project, some ideas in this work have been introduced to agree with likely manufacturing processes. One of the most important lens properties that has been discussed

is that it needs to be near-planar for unchallenging integration with the bulk substrates surrounding it. To illustrate this importance, an unrefined, example fabrication process is given here. Clarifying and utilising this process or similar is left as future work for the project.

Firstly, a layer of a-Si should be deposited onto the silica substrate with a thickness greater than that of the rods (> 1150 nm). Secondly, this layer should be etched down to the thickness of the rods. Next, unneeded a-Si should be etched away via an electron beam leaving only the nano-rods. Then, Si₀₂ should be deposited between and on top of the rods, to yield a planar surface with the rods buried beneath. This Si₀₂ surface should then be fused with the other silica substrate to complete the full length of the subsystem. As mentioned, the fused Si₀₂ layer is index-matched with the bulk glass substrates. Finally, this glass-lens-glass structure should be integrated with the DM-VCSEL and the UTC-PD.

As with any fabrication process, uncertainties are introduced. These are endeavoured to be minimised by the use of electron beam lithography which is capable of higher precision than many other lithographic processes [11]. The introduction of uncertainties may introduce scattering losses or potentially shift the focus point of the converging Gaussian beam after the lens. In an attempt to accommodate for the latter effect, the depth of focus of the lens (introduced in Section 2.2) should be sufficiently large such that any shifts in focal length are completely overshadowed by the large depth of focus. Of course, a large depth of focus means a larger focus point so there is again another trade-off that needs to be accounted for in the design of the system [11].

Another manufacturing uncertainty that needs to be accounted for is the misalignment of various components in the subsystem: the DM-VCSEL, the UTC-PD and the lens. While the misalignment of the DM-VCSEL and the UTC-PD has its challenges, this work mostly focuses on the impact of imperfections associated with the lens. More precisely, if the lens is misaligned with the other components such that its centre doesn't align well with the centre of the Gaussian beam, then astigmatic effects will be introduced into the beam focusing [7]. This is an important consideration due to the small diameter of the UTC-PD: any notable astigmatic effect could cause a significant drop in the amount of power coupled between the DM-VCSEL and the UTC-PD.

2.6 Subsystem Outline and Summary

Many ideas and concepts regarding the subsystem design were discussed throughout Section 2, with many of the ideas being dependent on one another. Therefore, this section serves to gather all of the appropriate ideas and system parameters to give an overall, holistic view. A schematic of the subsystem which supplements the outline here can be found in Figure 11.

First we give the parameters of the subsystem. Following the symbol representation of that in Figure 11 and in Section 2.2:

- $z_A = z_B = 400 \mu\text{m}$.
- $W_{0,A} = 5 \mu\text{m}$.

- $W_{0,B} = 2.5 \mu\text{m}$.
- Nominal beam frequency: 193.4 THz. Equal to a free space wavelength of $1.55 \mu\text{m}$.
- Initial beam Rayleigh length, $z_{0,A} = 72.9 \mu\text{m}$.
- Focused beam Rayleigh length, $z_{0,B} = 18.2 \mu\text{m}$.
- Focused beam depth of focus, $2z_{0,B} = 36.4 \mu\text{m}$.
- Focused beam waist at limit of depth of focus, $\sqrt{2}W_{0,B} = 3.53 \mu\text{m}$.
- Beam waist at lens, $W_A(z_A) = W_B(-z_B) = 27.9 \mu\text{m}$.
- Initial beam radius of curvature at lens, $R_A(z_A) = R$ (eq. (9)) = $413.3 \mu\text{m}$.
- Focused beam radius of curvature at lens, $R_B(-z_B) = R'$ (eq. (9)) = $-400.8 \mu\text{m}$.
- Phased array unit cell side length, $250 \mu\text{m}$.
- Bulk substrate material, silica, $n = 1.444$ at 193.4 THz [13].
- Nano-rod material, amorphous silicon, $n = 3.485$ at 193.4 THz [38].
- Focal length of lens from equation (10), $f = 203.5 \mu\text{m}$.
- Lens radius, $35 \mu\text{m}$.
- Number of rods, 6006.
- Lattice constant of rods, 800 nm .
- Rod diameters, 100 nm to 504 nm .

The phase profile that the lens is required to exert as a function of these parameters is given in Figure 9. The cross-section of the lens with length units is given in Figure 10. The Gaussian beam profiles at the DM-VCSEL aperture, the lens and the UTC-PD are depicted in Figure 8.

As discussed, nominal subsystem parameters are used in this project. They can be tailored to fit a more specified wider system design and can simply be inserted into the computer code used to design the lens. While nominal, many of these parameters closely represent values that may be found in the final system. As an example, typical high power VCSEL aperture diameters are typically between $5 \mu\text{m}$ and $10 \mu\text{m}$ [39], so the initial beam waist radius estimate of $5 \mu\text{m}$ is reasonable. Furthermore, modern UTC-PD designs typically have maximum diameters of $5 \mu\text{m}$, so the estimate of a focused beam waist of $2.5 \mu\text{m}$ is reasonable as to allow most of the beam power to couple into the UTC-PD [18]. Additionally, upon experiment with the simulation software CST, the parameters allow for a large number of rods to be simulated that is close to saturating the capabilities of the simulation software, hence the trade-off discussed at the end of Section 2.4 is appropriately balanced.

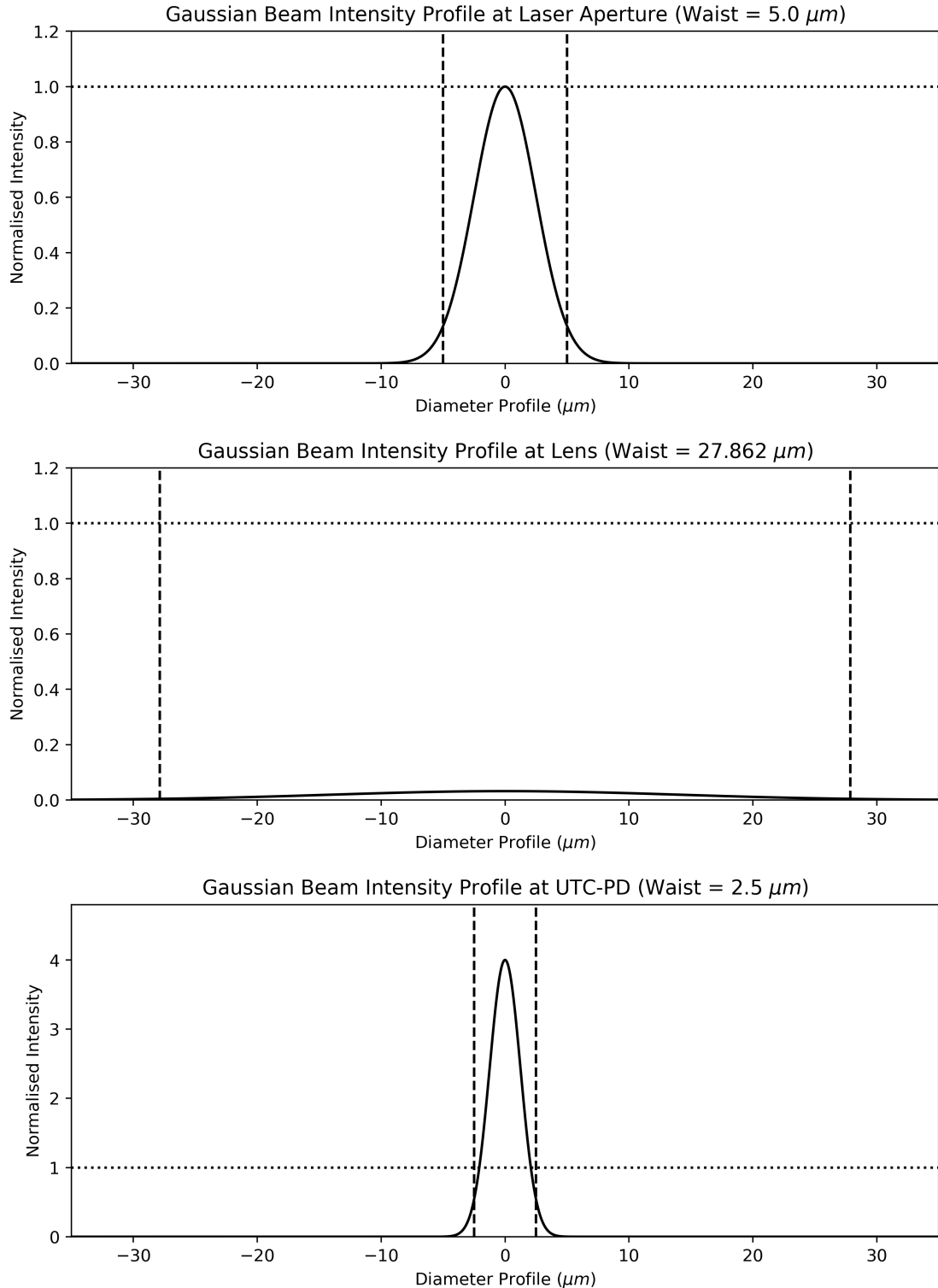


Figure 8: The intensity profiles of the Gaussian beams at the three most important points of interest, theoretically found. (top): The Gaussian beam intensity profile at the laser aperture. (middle): The beam intensity profile at the lens. (bottom): The beam intensity profile at the UTC-PD. In each of the figures, the vertical dashed lines demarcate the waist of the beam. Additionally, the horizontal dotted line marks where the peak intensity of the beam at the laser lies with respect to the other beams. These one-dimensional profile slices may appear to have varying total intensities (area under the curves), however, it is important to acknowledge that these are one-dimensional slices of two-dimensional functions. Across the full two-dimensional function, the total intensity remains constant across the three beam profiles.

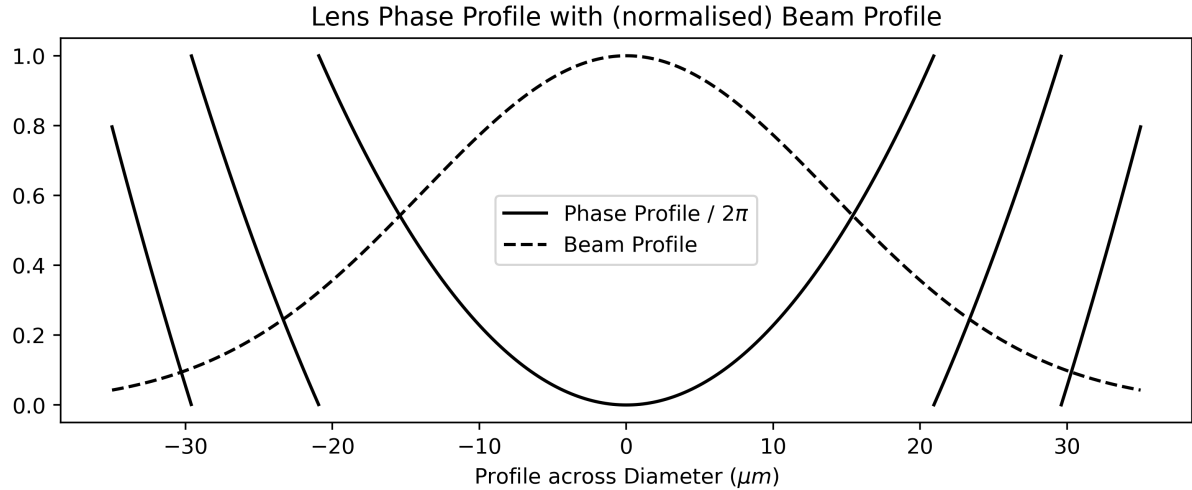


Figure 9: The dashed line in this figure displays a one-dimensional slice of the intensity profile of the initial Gaussian beam parameterised in Section 2.4 across the lens designed in Section 2. As the beam is Gaussian, most of the intensity (power) is concentrated near the centre. The solid black lines represent a one-dimensional slice of the rotationally symmetric phase profile that the lens needs to exert to agree with the subsystem parameters given in Section 2.6. Notably, the phase profile cyclically spans the range $(0, 2\pi)$. These $2\pi \rightarrow 0$ phase quasi-discontinuities manifest themselves as rod diameter discontinuities as can be seen in the final lens design shown in Figure 10.

Interestingly yet as expected, the focal length of the lens is $203.5 \mu\text{m}$. This is close to $200 \mu\text{m}$ which is the value that the focal length of the lens would be if the beam focuses were modelled at point sources, each $400 \mu\text{m}$ away from the lens [7]. This is expected as, outside of the Rayleigh lengths of the beams, $z_{0,A}$ and $z_{0,B}$, the beams can be considered to be in the far-field regime [11]. In this regime, Gaussian sources resemble point sources in terms of the wavefront shape only, not the intensity distribution. This is the reasoning behind why the focal length is similar to that of point sources except that it is slightly perturbed by the Gaussian nature of the sources. Therefore, for these system parameters, a point source approximation would likely have been upheld. However, a full Gaussian beam analysis is needed to ensure that the design workflow is capable of handling wildly varying system parameters that the finalised system may take, even if these parameters break the point source approximation.

3 Mapping Required Phase to Metasurface Elements

To be able to map the needed lens profile given in Section 2.6 to an actual design of the metasurface, a means by which to design each metasurface element to exert a given phase shift is required as eluded to in Section 2.4. Additionally, the phase shift provided by an a-Si rod in the metasurface is predominantly a function of the metasurface lattice constant, rod diameter and rod length. Therefore, for ease of manufacture, the lattice constant and rod length need to be decided and fixed such that the rod diameters can produce a phase function that cleanly spans the entire

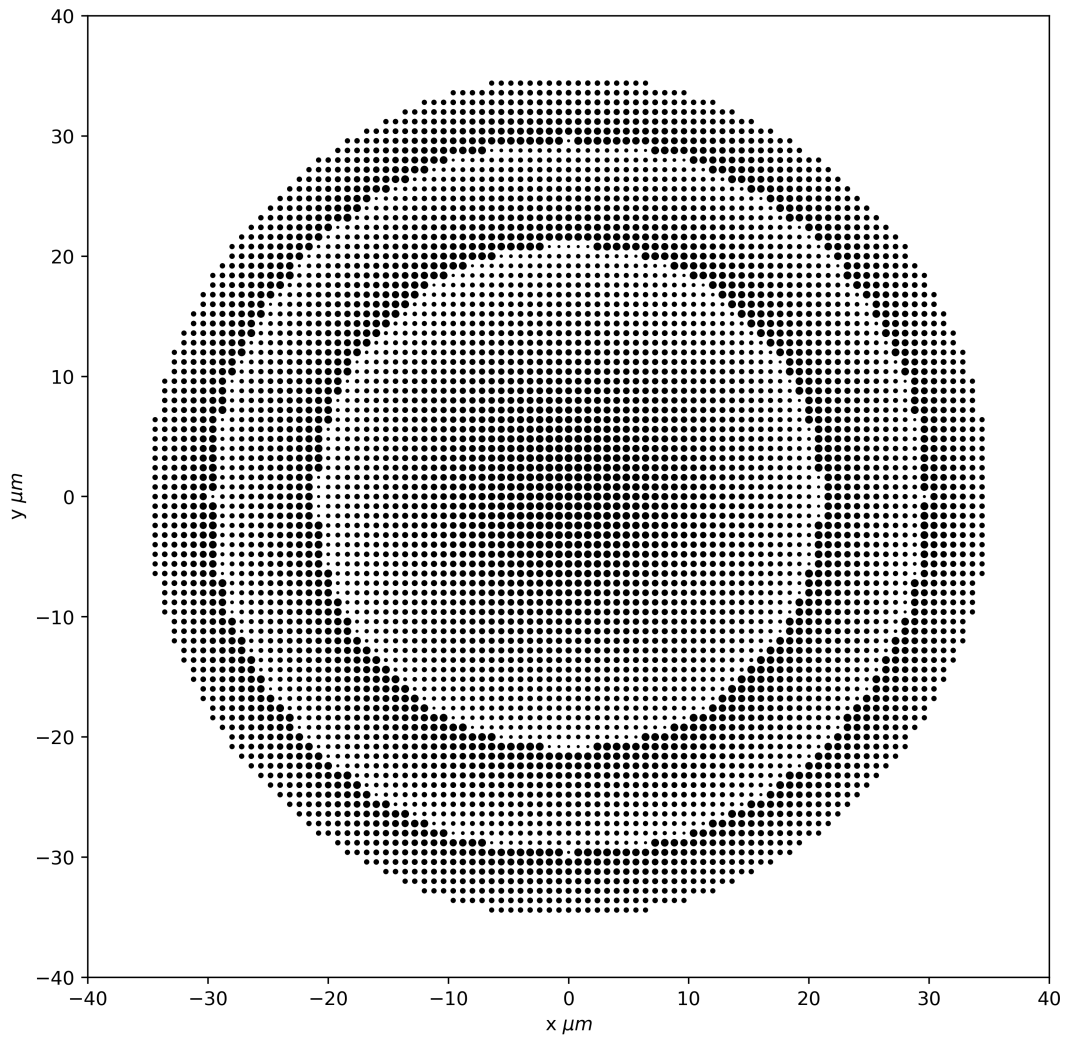


Figure 10: A plotted cross-section of the amorphous silicon rod based metalens designed in Section 2.4. Each rod is represented by a black dot of the same diameter. The radius of the lens is 35 μm .

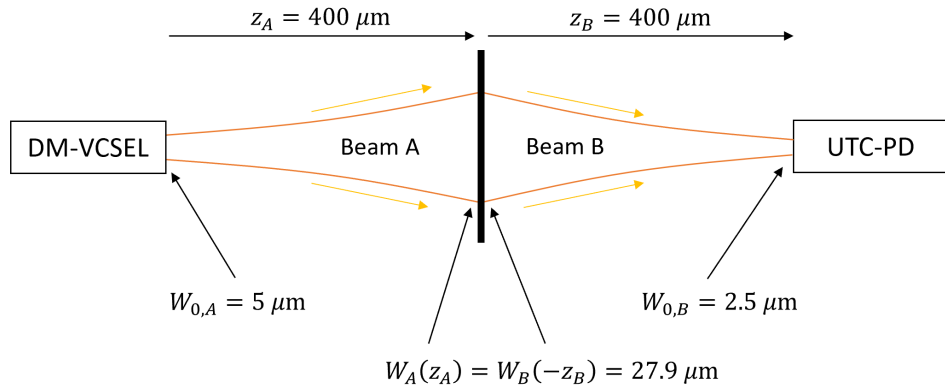


Figure 11: A parameterised summary of the subsystem designed throughout Section 2. The parameter symbols match those given in Section 2.6. The central black block represents the metalens.

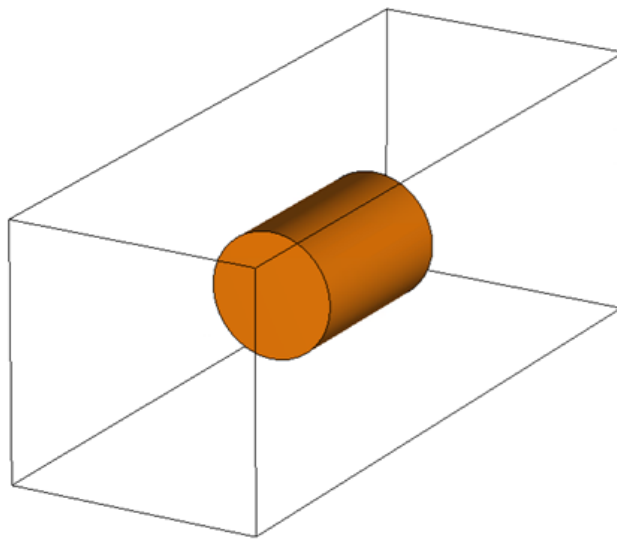


Figure 12: A single amorphous silicon rod embedded in silica surroundings. The wireframe rectangle is the infinite, periodic unit cell used in the simulations described in Section 3.

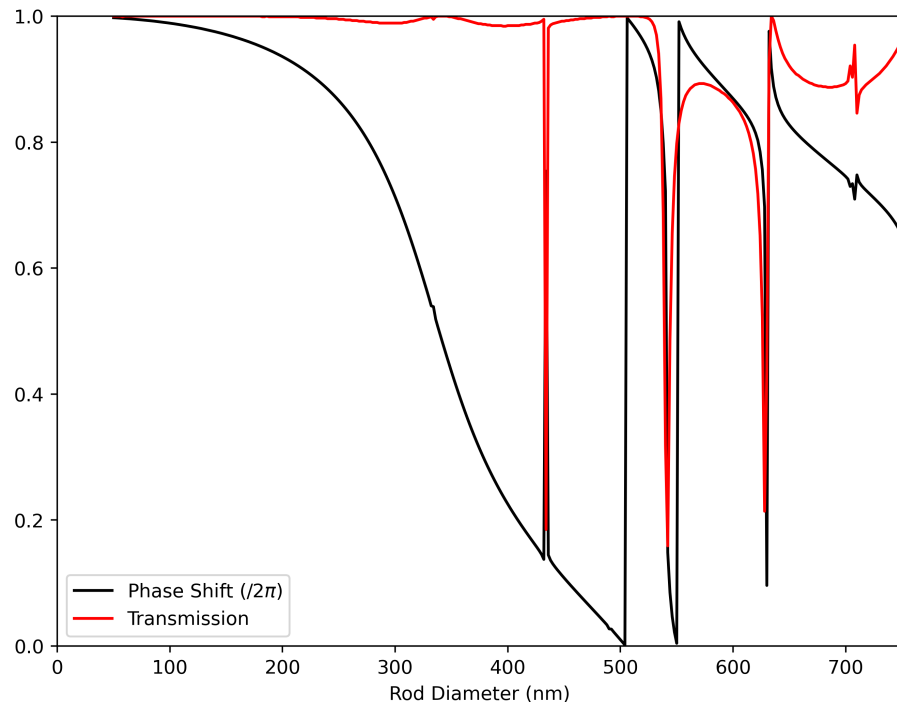


Figure 13: The phase shift (black) and transmission (red) provided by amorphous silicon rods of length 1150 nm and of varying diameter. The rods are evaluated with Floquet boundary conditions and are suspended in a silica background as detailed in Section 3.

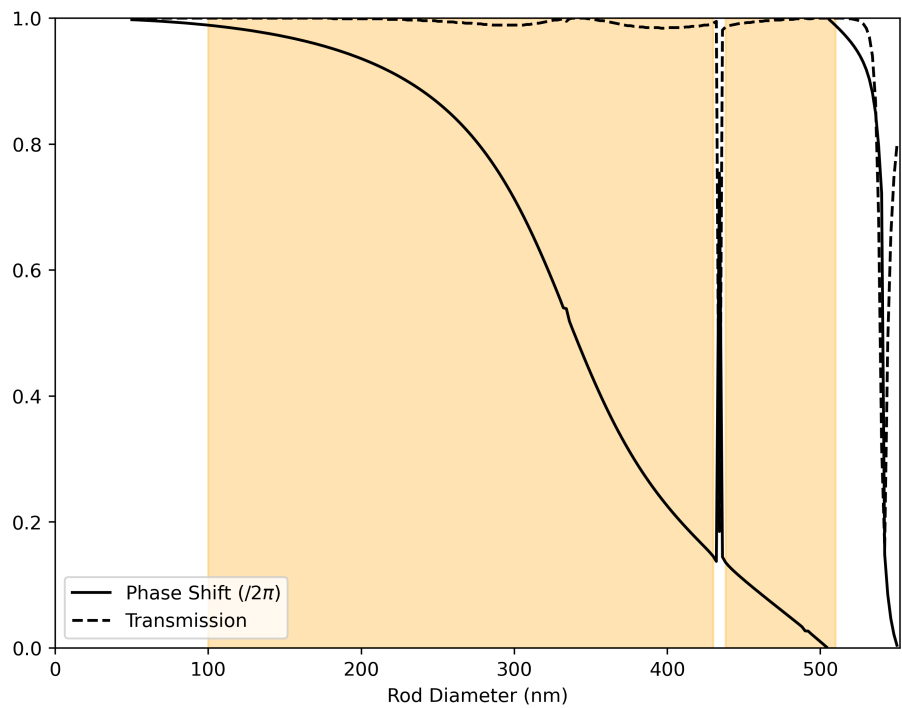


Figure 14: A subsection of Figure 13. Shown is the phase shift (solid black) and transmission (dashed black) as a function of rod diameter. The coloured section demarcates the range of rod diameters that were used to construct the metasurface designed in Section 2.4.

$(0, 2\pi)$ range.

To do this, the rod lattice constant was fixed to 800 nm as per Section 2.4 and many combinations of rod length and diameter were simulated to extract their phase shift on light with a frequency of 193.4 THz. The fixation lattice constant is further discussed in Section 5. In detail, the length parameter of the rods was evaluated between 500 nm and 1300 nm in steps of 50 nm. At every length tested, the diameter parameter was tested between 50 and 700 nm. Therefore in total, 2080 parameter combinations were simulated.

The details of the simulation for each combination are as follows. A single a-Si rod was placed in the simulation software CST, as per figure Figure 12. The rod was placed inside a rectangular bounding box of length 5 μ m and of square side length 800 nm, matching the lattice constant of the rods in the metalens. To attempt to quantify the scattering of the rod with external influences from surrounding rods, the bounding box was provided with infinite, periodic (Floquet) boundary conditions [11]. That is, the simulation is actually in the form of an infinite square lattice of identical rods. An infinite plane wave at 193.4 THz is then propagated through the infinite lattice and its phase shift away from the expected phase is measured at the far side of the bounding box.

The simulation of these rods is under the influence of two very important assumptions. Firstly, for a rod in the metalens, the four nearest neighbour rods are similar enough to it such that they can be modelled as identical rods. Rephrased, the lens phase profile is smooth enough such that adjacent rods exert similar enough phase profiles. This assumption is largely justified by the propagation of the beam such that it ‘experiences’ a near-continuum of rods following the trade-off discussion in Section 2.4. Additionally, the phase profile of the lens given in Section 2.6 is mostly smooth aside from the phase quasi-discontinuities as the necessary cycles from 2π back to 0. Of course, this is not a discontinuity in the phase as phase is cyclical mod 2π , it is a discontinuity in the rod diameter used as shown in Figure 10. This discontinuity is considered further in Section 5.

Another important approximation is that the infinite plane wave that the rods are subject to is a close enough approximation of the Gaussian beam section that a given rod is subject to in the subsystem. Two factors that may break this approximation are excessive curvature of the beam or an excessive gradient in intensity across the section of the beam. Efforts are made to reduce both of these effects by allowing the beam to propagate well past its Rayleigh length, again as justified by the trade-off discussion in Section 2.4.

With the rod diameter length and diameter sweep complete, each length was evaluated for its smooth, high transmission coverage of the phase range $(0, 2\pi)$. By an informed inspection, a length of 1150 nm was found to be the most optimal of those tested. Also, empirically, the longer lengths displayed a smoother phase coverage. This is reviewed further in Section 5. The phase shift and transmission of rods of length 1150 nm as a function of rod diameter between the full range tested is given in Figure 13. A subsection of Figure 13 is shown in Figure 14 in which is also shown the range of diameters that were chosen to map to their phase shifts in the range $(0, 2\pi)$.

Figure 13 shows that, for specific diameters at this length, the phase exertion and transmission can deviate significantly from their otherwise smooth profiles. These diameters are omitted from the

selection of rods that can be used to enact the phase profile. Simply, if that diameter is needed, the nearest stable diameter is used instead. The investigation as to why these phase discontinuities occur is beyond the scope of this project but some preliminary theories can be conjectured. For example, these discontinuities may be the result of an unwanted field resonance in or between the rods, or some higher-order coupling between a collection of rods. This is discussed further in Section 5.

Aside from avoiding these anomalous discontinuities, the rod range selected was also selected as such to agree well with potential fabrication methods. For example, although the minimum smooth rod diameter was 50 nm, the minimum rod diameter selected was 100 nm. The section of phase missed by omitting this range can be accounted for at the top end of the rod diameter-phase function, where the rod selection range was increased from 498 to 504. Remembering that the rods are 1150 nm long, a 50nm diameter rod provides an exceptionally thin rod with a diameter of approximately 4.3% of its length. A 100 nm rod doubles this ratio to 8.6%. This rod range selection shift could have been shifted further for more favourable length to diameter ratios however some phase discontinuities seem to appear above a diameter of 510 nm hence the maximum rod size is less than this, with a slight extra buffer. Additionally, and very importantly, the range was selected such that its transmission is high across the full range. In this case, the transmission is always $>95\%$.

4 Lens Design Evaluation

To evaluate the design workflow given in this work, we analyse the performance of a lens generated with this workflow with the parameters given in Section 2.6. To do this, we use the simulation software CST to propagate Gaussian beams through the lens and analyse how the beam behaves once subject to the lens. The result of this is shown in Figure 15.

Initially, a flaw with this approach must be acknowledged. Metasurfaces are by nature intricate - their feature sizes are smaller than the working wavelength [30]. Therefore, complex simulations are needed to emulate their properties well. This is an issue as, due to the complexity of the lens, only a very small portion of the subsystem was able to be simulated with the software. For example, while the length of the subsystem is 800 μm , only approximately 15 μm of ‘length’ inclusive of the lens. Due to the complexities of using CST, it was not possible during this project to ‘couple’ the simulation such that the region around the lens could be simulated initially and its results be extrapolated to the rest of the system by a subsequent simulation. This was attempted but not fully achieved as evidenced by Figure 16. Issues can arise when attempting this ‘coupled’ simulation technique due to a discontinuity in the computational cell mesh density between the two simulations [11]. This can lead to undesired and unphysical effects such as refraction and reflection at these discontinuities [11]

Therefore, as a limited but promising workaround to this issue, the diverging and converging Gaussian beams before and after the lens respectively were computationally mapped to their theoretical description given by equation (3). However, to account for the fact that the position of the focus is a free parameter, equation (3) was modified as follows to include this global offset in the z direction, z_{off} :

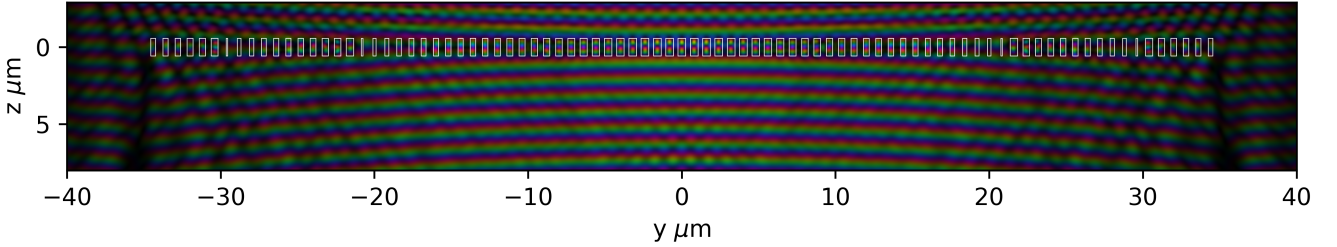


Figure 15: A two-dimensional slice through the initial and resultant Gaussian beams as the initial passes through the metalens design. The initial beam is incident on the lens from the negative z direction and the resultant beam continues in the positive z direction. Colour represents the electric field phase and colour intensity represents its magnitude. The colour intensity is normalised to the electric field magnitude which is maximal in the rods. The white rectangles are lateral cross-sections of the ‘rods’ in the metalens structure, in which the field localisation discussed in Section 2.3 can be observed. The lens apertures only part of the initial beam such that the initial beam can be seen to continue diverging out of the shadow of the lens. Meanwhile, the portion of the initial beam subject to the lens begins to converge as shown by its change in radius of curvature with respect to the initial beam.

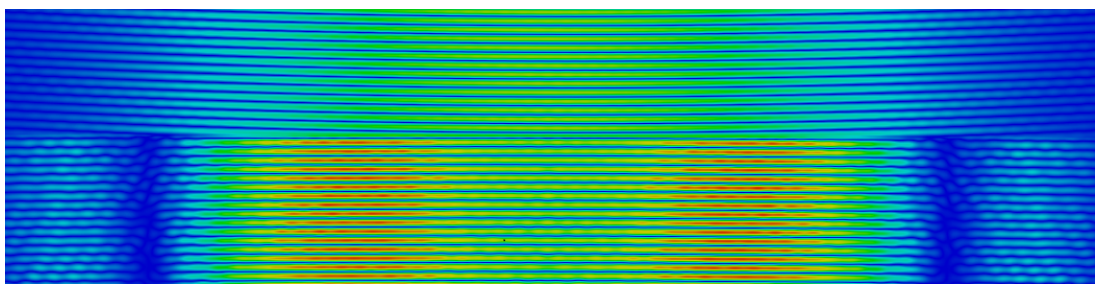


Figure 16: A cross-sectional plot of the results of an attempted ‘coupled’ simulation, the premise behind which is given in Section 4. The top half is the result of one Gaussian beam simulation which is then passed to the lower half which is run as part of a separate simulation. The mesh discontinuity and other unphysical factors are apparent as the beam changes intensity profile, changes radius of curvature and acquires side-lobes reminiscent of a Bessel beam. In theory, none of these changes should occur - it should be a seamless transition.

Parameter	Fitted	% Uncertainty
λ	$1.0598 \pm 0.0008 \mu\text{m}$	0.075
W_0	$6.861 \pm 0.092 \mu\text{m}$	1.34
z_{off}	$402.01 \pm 3.74 \mu\text{m}$	0.93

Table 1: A summary of the parameters of interest found during the fitting of the Gaussian beams in Figure 17, their uncertainties as estimated by the fitting procedure and their subsequent percentage uncertainties.

$$U(\mathbf{r}) = A_0 \frac{W_0}{W(z - z_{\text{off}})} \exp\left(-\frac{\rho^2}{W^2(z - z_{\text{off}})}\right) \exp\left(-jk(z - z_{\text{off}}) - j\frac{k\rho^2}{2R(z - z_{\text{off}})} + j\xi(z - z_{\text{off}}) + \phi_{\text{off}}\right) \quad (11)$$

where ϕ_{off} is a global phase offset to account for the fact that the beam will very likely exist at zero phase at its focal point. Therefore, there are five free parameters that must be numerically evaluated: A_0 , W_0 , λ , z_{off} and ϕ_{off} . The Rayleigh length z_0 can then be found from W_0 and λ by equation (7).

To numerically fit the Gaussian beams found by simulation to equation (11), the scientific computing package *scipy* was used to perform a non-linear least-squares fit [40]. Notably, this is a heuristic optimisation technique analogous to gradient descent and is therefore vulnerable to local minima and highly sensitive to an initial guess of the fitting parameters. These issues are incredibly important to the analysis of the performance of the lens here. As the incident Gaussian beam is subject to the intricate metasurface, it is subject to ‘noisy’ deviations from a perfectly Gaussian shape which also propagate as the beam propagates - they are largely persistent. Additionally, as only a small section of the subsystem can be simulated, the fitting function is potentially not provided with enough information to find an informed fit of the data to the Gaussian beam function. These issues manifest in the analysis below and are further discussed as appropriate.

With an introduction to the method by which we analyse the performance of the lens given, we now employ this method, the results of which are given in Figure 17. The parameters extracted from the least-squares fitting procedure are given in Table 1.

With these results found, discussion can follow regarding the fitting procedure, the results and the performance of the lens and how these quantities are linked. First, an important discussion is to be had regarding the uncertainty of these results. The uncertainty was found by yielding the standard deviation in parameter estimate as returned by the non-linear least-squares fitting function [40]. For example, for the wavelength λ value found and given in Table 1, the ‘uncertainty’ is a fraction of a nanometre at $0.0008 \mu\text{m}$ even though it deviates from the expected value as to be detailed further below. Similar effects are seen across all of the found parameters. This could be interpreted as the fitting function converging deep into a local minima of the fitting function such that the uncertainties are small. Colloquially, it is confidently incorrect. This is tied to the discussion earlier in this section regarding the vulnerability of the fitting functions to local minima. On empirical experimentation, this vulnerability is very apparent - slight deviations in the initial state of the fitting function led to differing results, some of which were even diverging numerical instabilities. Due to the local

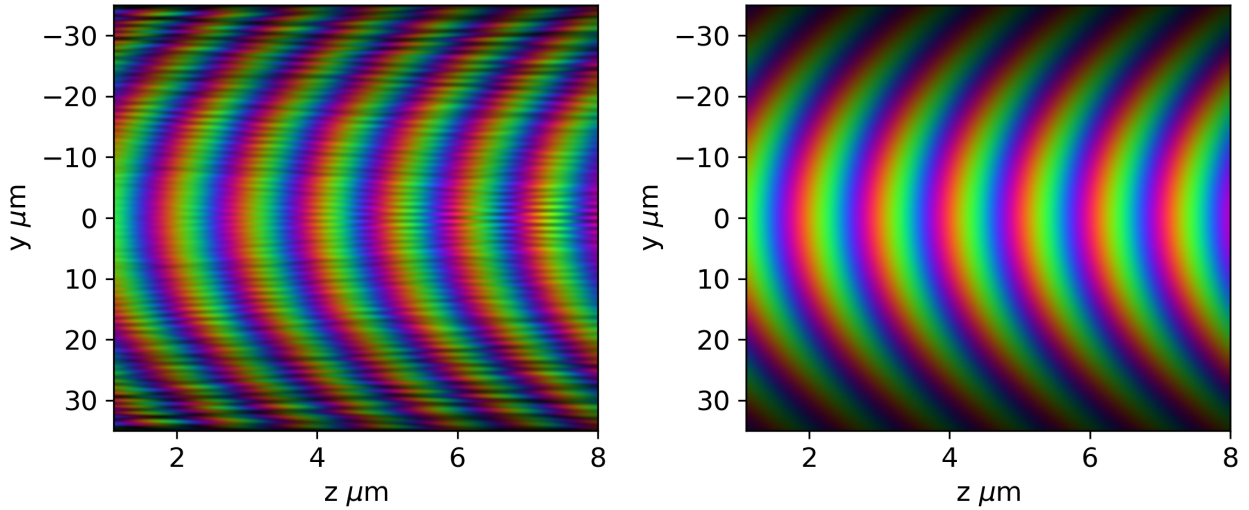


Figure 17: (left): A two-dimensional cross-section of the electric field emergent from the metalens which continues to propagate in the positive z direction. The lens is not pictured and is situated at $z = 0 \mu\text{m}$. The intensity of colour represents the magnitude of the complex electric field value and the colour itself represents its phase. (right): A plot of the modified Gaussian beam equation (equation (11)) evaluated with the parameters found from the non-linear least-squares fitting procedure, given in Table 1. The colour intensity distribution is altered slightly across the original and fitted beams as the colours are normalised to the largest electric field magnitude value which is higher in the left figure due to noise in the beam introduced by the scattering metasurface. Both of these plots are only evaluated inside the shadow of the lens, even though the simulation was carried out outside of this frame as shown in Figure 15. This was done such that the non-apertured field would not interfere with the fitting procedure outlined in Section 4.

minima vulnerability and the sensitivity of the initial condition, we can propose another type of ‘effective uncertainty’ due to the cumulative effect of these issues. Empirically, it was found that the wavelength found could deviate by as much as $1.5 \mu\text{m}$. While this is not a rigorously found value, it is an indication that such an ‘effective uncertainty’ exists. To attempt to reason with this, the fitting function was run many times with many different initial conditions. The ‘result’ found was the parameter set that provided the least cumulative percentage uncertainty across the parameters. While this of course takes into account that the parameters operate in different unit regimes, it does not take into account that some parameters are not linearly independent such as λ and W_0 . Therefore, while efforts have been made to account for the simulation limitations and the limitations of the beam fitting procedure, these results cannot be fully reasoned to be accurate and hence should be viewed with some scepticism. Somewhat more reliable results regarding the focussing of a plane wave are compared to these in Section 4.1.

With this scepticism in mind, we can analyse the result for each parameter and consider the validity of the fitting procedure in each case. First, we discuss the wavelength, which was briefly discussed in the previous paragraph. The measured wavelength ($1.060 \mu\text{m}$) deviates by 1.67% from the expected wavelength which is the free space wavelength divided by the refractive index of the silica substrate, $\lambda = \frac{\lambda_0}{n} = 1.076 \mu\text{m}$. Additionally, this value lies outside of the $0.0008 \mu\text{m}$ uncertainty returned by the fitting algorithm. Furthermore, as briefly mentioned, it discrepancy could be due to the dependence on the W_0 parameter as shown in equation (7). The reason that the measurement lies outside of the acceptable uncertainty range could be due to the factors considered early in this section regarding the ‘effective uncertainty’ due to the fitting function. The reason the algorithm returns such a small uncertainty in the fit is likely because the beam oscillates several times in the simulated area. This allows a fitting function to well infer the wavelength.

Secondly, we discuss W_0 . The measured value ($6.861 \mu\text{m}$) is significantly larger than the expected value of $2.500 \mu\text{m}$. In addition, similarly to λ , the expected value is outside the uncertainty range of the measured value. This measurement likely suffered for similar reasons that the λ measurement suffered. Additionally, it is possible that this measurement also suffered because the beam’s waist varies very slowly across the measured profile. That is, the fitting function is unable to extrapolate this beam waist variation accurately to approximately $400 \mu\text{m}$ further.

Finally, we analyse the z_{off} measurement which is exactly a measurement of how far along the z direction the focus of the beam is with respect to the lens. As introduced in Section 2.2, this quantity is not the focal length of the lens. This quantity is measured to be $402.01 \pm 3.74 \mu\text{m}$ and is, therefore, the only variable in which the uncertainty range extends to the expected value, being $400 \mu\text{m}$. This measurement was likely somewhat successful due to the same reason that the λ measurement was partially successful: there are several full-wave oscillations in the measured slice. That is, the fitting function has several attempts at ‘measuring’ the radii of curvature. With these ‘measurements’, it is more viable to more accurately measure z_{off} .

4.1 Focusing Accuracy Further Discussion

Although the successful z_{off} measurement given previously has been discussed, the designing of a lens structure suggests that its focusing properties should be studied further.

To measure the focal length f of the lens, a plane wave was passed through the lens as shown in Figure 18. Analogously, the result was fit to the theoretical function that should describe its behaviour. In this case, we expected a converging beam with spherical wavefronts, so we fit the phase $\phi(r)$ only of the beam to

$$\phi(r) = kr + \phi_{\text{off}} \quad (12)$$

where r is the radius of a point from the centre of the focus, $r^2 = y^2 + (z - z_{\text{off}})^2$. Note that this is essentially the two-dimensional magnitude of the vector \mathbf{r} used in equation (11). In equation (12), $k = \frac{2\pi}{\lambda}$ and ϕ_{off} represents the same entity as in equation (11).

The same fitting procedure employed for the Gaussian beam was then used. That is, the fit with the minimal total percentage uncertainty was deemed the ‘result’. The wavelength λ measured from this procedure was found to be $1.06052 \pm 0.00006 \mu\text{m}$. This measurement again deviates from the expected wavelength of $1.076 \mu\text{m}$ but is remarkably similar to the λ measured by the Gaussian beam simulation. Although again, the uncertainty returned is incredibly small which is likely to be as such for similar reasons as the measurement from the Gaussian beam. These similar yet incorrect λ measurements could imply that there is potentially an unexpected behaviour with which the simulation software CST handles its refractive index as a function of permittivity and permeability - clarification would require further investigation.

The $z_{\text{off}} = f$ measurement was found to be $204.05 \pm 0.03 \mu\text{m}$ which is remarkably comparable to the expected $f = 203.5 \mu\text{m}$. However, the expected value lies outside of the found uncertainty range even though it is only 0.49% out. Although, it is reasonable to postulate that the measurement is inside the ‘effective uncertainty’ range earlier discussed in Section 4 which is due to complications with the fitting procedure and the limited size of the simulation.

Overall, the measurements made on the plane wave simulation performed better than the measurements made on the Gaussian beam simulation, both in terms of accuracy and uncertainty. This could potentially be due to the simplicity of the fitted function used in the case of the plane wave, equation (12). In this function, all of the variables are linearly independent. This could be further evidence that the inter-dependency of λ and W_0 in the Gaussian beam fitting process is problematic for the beam fitting process.

Next, we further analyse the focusing ability of the lens by investigating dispersive effects. In the context of lensing, dispersive effects manifest as chromatic aberrations [7]. This is crucial to investigate as, as eluded to in Section 2.3, bandwidth is often limited in metlenses [30]. While the operation of the lens will deviate from the expected eventually as the frequency changes, it is important that the focusing and transmission behaviour remains consistent enough within the range of 300 GHz as this is the photomixing frequency used in the subsystem. To ensure this range is well analysed, five Gaussian beams of constant W_0 were simulated with frequencies from 192.6 THz to

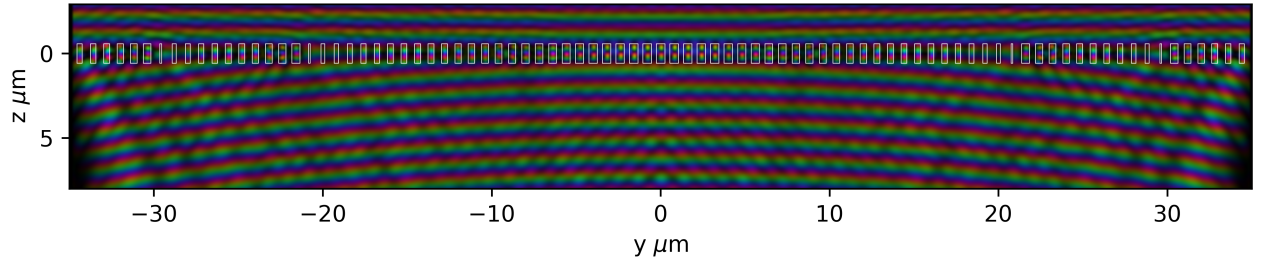


Figure 18: A two-dimensional slice through an initial plane wave incident on the metasurface and its resultant converging beam in exact analogy to the contents of Figure 15.

194.2 THz. This range spans 1.6 THz and is centred on the nominal VCSEL operation frequency of 193.4 THz.

Upon fitting the simulated beams with the same procedure as considered throughout this section, the results shown in Figure 19 were found. It is important here to note that ideally but impossibly, it is desirable for all frequencies to behave exactly at 193.4 THz, not as each frequency itself should physically behave. That is, all frequencies measured should focus on the same point. Following the results shown, it can be seen that the z_{off} values for all frequencies overshoot the mark. This is further evidence of a currently unknown systematic error with the simulations perhaps to do with the refractive index as first mentioned in Section 4.1. Interestingly, a clear negative, potentially linear correlation is shown. This is strong evidence to show that the behaviour of the lens deviates with respect to frequency but at least deviates somewhat consistently. It should be noted that the uncertainties shown are the uncertainties from the fitting procedure, not the ‘effective uncertainty’ from the limitations of the fitting procedure. Additionally, the higher uncertainties associated with the lowest and highest frequency points potentially indicate that these are reaching the edge of the operational band of the metasurface - more simulation is needed. Finally, and most importantly, the deviations in z_{off} remain within 15% of the theoretical depth of focus given in Section 2.6; implying that the beams do not excessively deviate such that they would slip out of focus at the focus. In short, the 300 GHz separated photomixing beams would not experience a significant deviation in focal length for anywhere in the range of 192.6 THz to 194.2 THz.

4.2 Power Coupled

While we have, aside from the potential unreliability of the beam fitting procedure, found that the focal length of the beam does not significantly deviate to go beyond the desired depth of focus. This is only one part of ensuring that the power coupled from the DM-VCSEL to the UTC-PD is a large proportion and remains that way for a 300 GHz frequency spread. As the deviations in focal length are small with respect to the depth of focus, we can assume that the beams measured are in focus at the UTC-PD aperture. Additionally, we will assume that the diameter of the UTC-PD encapsulates the entire profile of the beam - the beam is not apertured by the UTC-PD. These assumptions

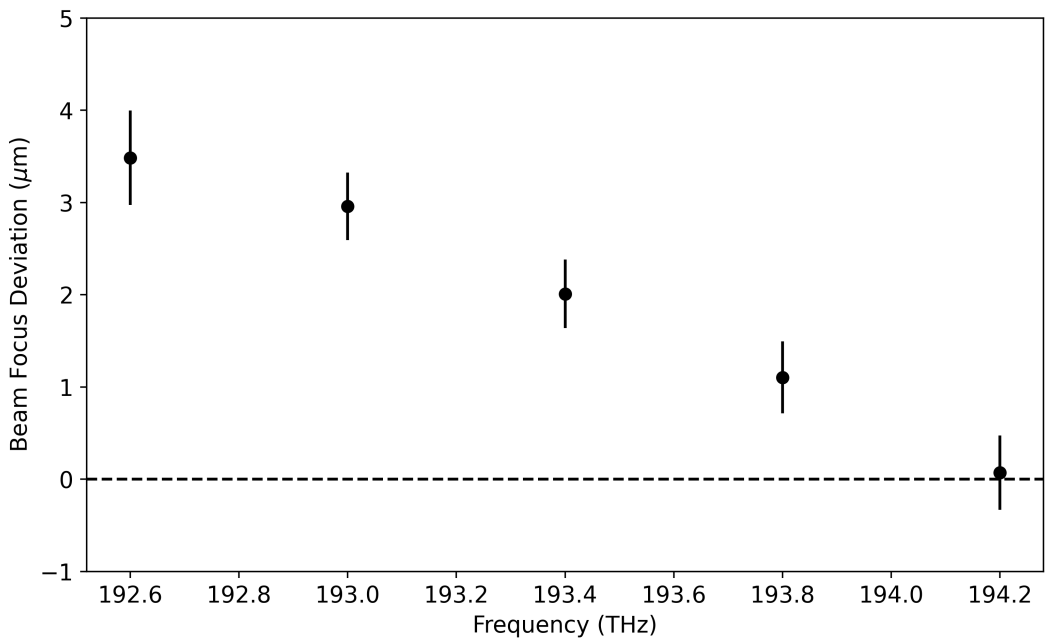


Figure 19: The deviation of z_{off} from its desired value of 400 μm is measured against the frequency of the simulated Gaussian beam used in the subsystem. All other subsystem parameters are kept constant throughout all measurements. Each point has error bars attached which denote the uncertainty found from the fitting procedure used throughout Section 4. The nominal working frequency of the VCSEL is the central-most point, 193.4 THz. The dotted line is where, ideally, all points would lie.

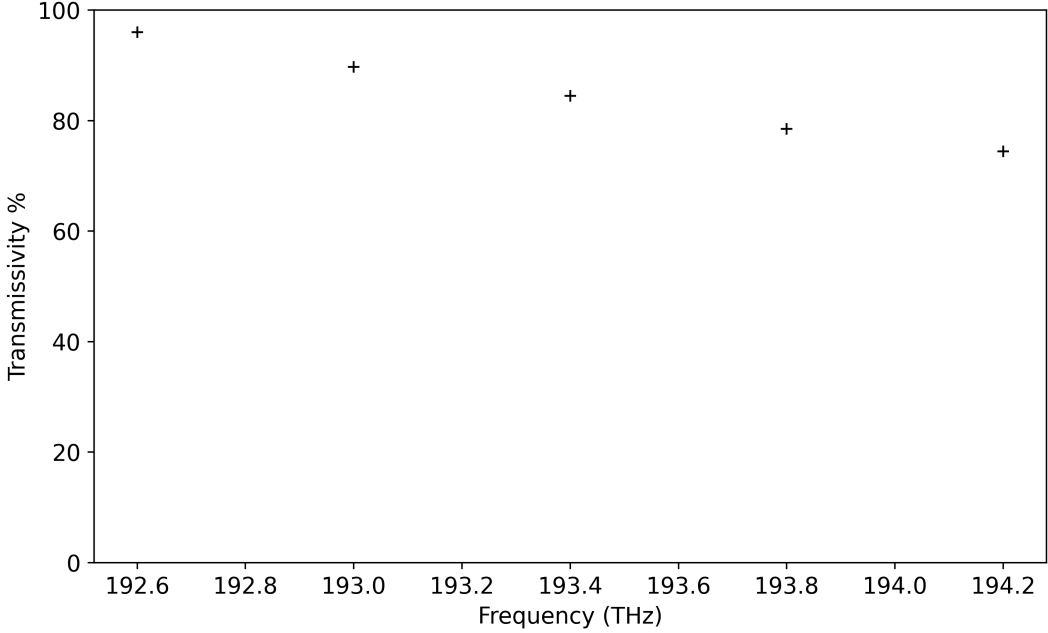


Figure 20: The power transmission of the designed metasurface as a function of the frequency of the simulated Gaussian beam passing through it.

simplify the power coupling dispersive effects which is practical considering that finding the focal waist W_0 reliably has not been achieved as outlined in Section 4.1. Removing these assumptions remains part of the future work for this project.

By numerically integrating the power profile with Simpson’s rule as implemented in *scipy* before and after the lens within the shadow of the lens only, the power transmissivity of the lens can be measured [40]. The results of this for the frequency range 193.6 to 194.2 THz are shown in Figure 20. For full clarity, integrating only in the shadow of the lens means that the power lost due to the beam being apertured by the lens is not taken into account. A larger lens can be designed to mitigate this power loss if necessary.

Analysing the results shown in Figure 20, we find that the power transmissivity decreases with frequency from a maximum value of 96.01% to a minimum of 74.45%. Notably, these values are generally lower than the rod transmissivities given in Section 3 which were always above 95%. This discrepancy is potentially due to the curvature of the beam which may be pushing the boundaries of the paraxial approximation assumed in Section 3. This is further evidenced by the fact that the transmission decreases as a function of frequency. Due to (7), the Rayleigh length z_0 of a beam is proportional to its frequency, $z_0 \propto f$. The quantity z_0 is a measure of the divergence hence the curvature of the beam [11]. Therefore, beams with higher frequencies will have smaller radii of curvature at the lens and hence conform less to the paraxial approximation.

While the transmission is comparable to or slightly lower than other microlens designs for the sub-THz range, the transmissivity is not significantly affected by a shift in frequency by 300 GHz [30, 41]. These results imply that photomixing with lower frequencies, closer to 192.6, may be

favourable with this lens design but its feasibility depends on the capability of the DM-VCSEL design. This investigation remains as further work for the project.

4.3 Lens Evaluation Summary

This project aimed to propose a microlens design to fulfil two objectives. The first of which is unchallenging planar integration with the subsystem described in Section 2. The second objective is for the lens to effectively couple power from the DM-VCSEL to the UTC-PD. A prerequisite to the latter is that the lens can focus the beam accurately.

For the first key challenge, a planar design, the design process given in Section 2.3 and Section 3 was proposed. Lenses designed via this process are reasonably straightforward to fabricate as discussed in Section 2.5, especially with respect to their non-planar counterparts. The design workflow is also able to be fully parameterised such that the design of the wider subsystem is not limited to the nominal parameters used in this work. As an example, the design workflow can produce lenses that focus beams with differing waists as is the case in the lens example studied in this work. In this sense, a large part of the meaningful results of this project is the design workflow itself.

Needless to say, the lens design workflow is ultimately evaluated by the lenses it produces. To this end, a lens was designed and assessed. It was found that the lens focused nearly as expected, to within 2% for the nominal frequency of 193.4 THz. Additionally, the dispersive effects of the focal distance of the beams were found to be small, up to a maximum of 15% of the depth of focus. By the analysis of a plane wave incident on the lens, it was found that the lens did operate at the designed focal length to within 0.5 μm , or 0.125%. Additionally, the power transmissivity of the lens was found to deviate up to a maximum of 20% while largely remaining above 75% even though the range tested was over five times wider than the needed bandwidth of 300 GHz.

One key drawback of the analysis in the approach was the beam fitting technique hence the results above should be viewed with some doubt. Fortunately, this is not an issue with the lens design process itself but just the evaluation of the lens. It was found that this fitting process was potentially unreliable due to several factors including the limited size of the simulation.

5 Future Work

Concerning this work, the most obvious first point to address is the beam fitting technique or other means to extrapolate the beam across the entire subsystem. Potentially a more rigorous optimisation technique such as simulated annealing could be used. Although, ideally, a full simulation of the subsystem would be made possible. If neither of these are possible, then the ‘effective uncertainty’ associated with the local minima sensitive fitting function could be well quantified and accounted for.

There are some aspects of the rod structures that should be further investigated. Firstly, the lattice constant of the rod lattice is a parameter that could be explored further. Investigations

should take place into the ramifications of the rod diameter discontinuities at the $0 \rightarrow 2\pi$ phase quasi-discontinuities, although by inspection their effect appears to be minimal. Also, a further investigation as to why longer rods tend to give broader, smoother phase coverage would be useful.

With regard to the lens itself, some assumptions are yet to be challenged. The first is that the emergent beam is well modelled by a Gaussian beam. Additionally, the lens is assumed to be polarisation invariant but may not be due to the square lattice - the lens is not rotationally invariant. Although, other, similar work claims polarisation invariance [30]. Additionally, the lens, the DM-VCSEL and the UTC-PD may not be perfectly aligned on the same optical axis, hence astigmatic effects should be explored.

Lastly, and less in the scope of this project, are more considerations of the wider system. Firstly, the DM-VCSEL design will be highly non-trivial and potentially the emitted beams may not be approximated well by a Gaussian beam [39]. Secondly, and incredibly importantly, how phase modulation is enacted needs to be fully investigated. As, of course, precise and fast phase modulation is needed for a collection of these subsystems to perform beam steering as discussed in Section 1. There are three points at which the phase may be modulated: the DM-VCSEL, the lens and the UTC-PD. A simple prototype may be to perform on-off keying by modulating the bias across the UTC-PD which can be controlled at very high rates [11]. A potential means to achieve phase modulation may be to integrate the metasurface with a bulk, electrically modulated phase change material or an active metasurface [42, 43, 44, 45]. In modulating the phase at the lens, the signal generation (at the DM-VCSEL) and the signal modulation (at the lens) are separated.

Finally, other considerations of the wider system will have to be explored. For example, refining the antenna design. More complexly, consideration will have to be given to the metal tracks needed to pump the DM-VCSEL and to potentially modulate the phase at the lens level.

6 Conclusion

This project set out to design a lens as part of a wider THz photomixing subsystem. The lens design had to couple power effectively between the DM-VCSEL and the UTC-PD as well as, ideally, be able to planarly fuse with two bulk substrates for high throughput manufacturing. As discussed at length in Section 4, these objectives were met by the nominal lens design given in this work. Additionally, the entire design workflow developed here can be fully parameterised for future designs. The design workflow was also compared against a more classical approach: Fresnel lenses.

The insights gained from this project should inform future work regarding the design of the entire beam steering system, especially if the alterations and improvements discussed in Section 5 are considered. Therefore, this work may contribute directly to the first 300 GHz, high-power, large scale transmitter appropriate for high data rate short-to-medium range communications - a niche which currently remains unmet.

References

- [1] T. Nagatsuma, G. Ducournau, and C. C. Renaud, “Advances in terahertz communications accelerated by photonics,” *Nature Photonics*, vol. 10, no. 6, pp. 371–379, 2016.
- [2] S. S. Dhillon, M. S. Vitiello, E. H. Linfield, A. G. Davies, M. C. Hoffmann, J. Booske, C. Paoloni, M. Gensch, P. Weightman, G. P. Williams, E. Castro-Camus, D. R. S. Cumming, F. Simoens, I. Escoria-Carranza, J. Grant, S. Lucyszyn, M. Kuwata-Gonokami, K. Konishi, M. Koch, C. A. Schmuttenmaer, T. L. Cocker, R. Huber, A. G. Markelz, Z. D. Taylor, V. P. Wallace, J. Axel Zeitler, J. Sibik, T. M. Korter, B. Ellison, S. Rea, P. Goldsmith, K. B. Cooper, R. Appley, D. Pardo, P. G. Huggard, V. Krozer, H. Shams, M. Fice, C. Renaud, A. Seeds, A. Stöhr, M. Naftaly, N. Ridler, R. Clarke, J. E. Cunningham, and M. B. Johnston, “The 2017 terahertz science and technology roadmap,” *Journal of Physics D: Applied Physics*, vol. 50, no. 4, p. 043001, 2017.
- [3] H.-J. Song, K. Ajito, Y. Muramoto, A. Wakatsuki, T. Nagatsuma, and N. Kukutsu, “Uni-Travelling-Carrier Photodiode Module Generating 300 GHz Power Greater Than 1 mW,” *IEEE Microwave and Wireless Components Letters*, vol. 22, no. 7, pp. 363–365, 2012.
- [4] “Cisco Annual Internet Report - Cisco Annual Internet Report (2018–2023) White Paper,” 2021.
- [5] “IEEE Standard for High Data Rate Wireless Multi-Media Networks—Amendment 2: 100 Gb/s Wireless Switched Point-to-Point Physical Layer,” IEEE, Tech. Rep.
- [6] M. Fujishima, “Future of 300 GHz band wireless communications and their enabler, CMOS transceiver technologies,” *Japanese Journal of Applied Physics*, vol. 60, no. 3, p. 803, 2021.
- [7] E. Hecht, *Optics*. Boston: Pearson Education, 2017.
- [8] P. F. McManamon and A. Ataei, “Progress and opportunities in the development of nonmechanical beam steering for electro-optical systems,” *Optical Engineering*, vol. 58, no. 12, p. 1, 2019.
- [9] M. Tani, P. Gu, M. Hyodo, K. Sakai, and T. Hidaka, “Generation of coherent terahertz radiation by photomixing of dual-mode lasers,” *Optical and Quantum Electronics*, vol. 32, no. 5, pp. 503–520, 2000.
- [10] T. Ishibashi and H. Ito, “Uni-Traveling-Carrier Photodiodes,” *Journal of Applied Physics*, vol. 127, no. 3, p. 031101, 2020.
- [11] B. E. A. Saleh and M. C. Teich, *Fundamentals of photonics*. New York: Wiley, 1991.
- [12] M. Hossain, S. Boppel, W. Heinrich, and V. Krozer, “Efficient active multiplier-based signal source for >300 GHz system applications,” *Electronics Letters*, vol. 55, no. 23, pp. 1220–1221, 2019.
- [13] C. Tan, “Determination of refractive index of silica glass for infrared wavelengths by IR spectroscopy,” *Journal of Non-Crystalline Solids*, vol. 223, no. 1-2, pp. 158–163, 1998.
- [14] G. Ducournau, P. Sriftgiser, T. Akalin, A. Beck, D. Bacquet, E. Peytavit, and J. F. Lampin, “Highly coherent terahertz wave generation with a dual-frequency Brillouin fiber laser and a 1.55 μm photomixer,” *Optics Letters*, vol. 36, no. 11, pp. 2044–2046, 2011.

- [15] R. Paquet, S. Blin, M. Myara, L. Le Gratiet, M. Sellahi, B. Chomet, F. Pavanello, P. Latzel, G. Ducournau, I. Sagnes, G. Beaudoin, and A. Garnache, “Coherent THz generation based on a novel dual-frequency III-V semiconductor laser,” in *2016 41st International Conference on Infrared, Millimeter, and Terahertz waves (IRMMW-THz)*, Copenhagen, 2016, pp. 1–2.
- [16] L. G. Guerrero, C. Graham, J. George, C. Renaud, G. George, B. Hussain, H. M. Salgado, L. M. Pessoa, A. Hinojosa, J. Fernandez, and M. A. G. Porcel, “Design and Fabrication of sub-THz Steerable Photonic Transmitter 1×4 Array for Short-Distance Wireless Links,” in *2021 Joint European Conference on Networks and Communications*, Porto, 2021, pp. 490–495.
- [17] E. Rouvalis, C. C. Renaud, D. G. Moodie, M. J. Robertson, and A. J. Seeds, “Traveling-wave Uni-Traveling Carrier Photodiodes for continuous wave THz generation,” *Optics Express*, vol. 18, no. 11, p. 11105, 2010.
- [18] H. Ito, T. Furuta, S. Kodama, and T. Ishibashi, “InP/InGaAs uni-travelling-carrier photodiode with 310 GHz bandwidth,” *Electronics Letters*, vol. 36, no. 21, p. 1809, 2000.
- [19] T. Ishibashi, Y. Muramoto, T. Yoshimatsu, and H. Ito, “Unitraveling-Carrier Photodiodes for Terahertz Applications,” *IEEE Journal of Selected Topics in Quantum Electronics*, vol. 20, no. 6, pp. 79–88, 2014.
- [20] T. Wahyudi, C. Apriono, F. Y. Zulkifli, and E. T. Rahardjo, “Broadband planar bow-tie antenna on high resistivity silicon substrate for terahertz application,” in *2017 15th International Conference on Quality in Research (QIR) : International Symposium on Electrical and Computer Engineering*, Nusa Dua, 2017, pp. 372–376.
- [21] C. P. Wong, Ed., *Polymers for electronic and photonic applications*. Boston: Academic Press, 1993.
- [22] K. B. Sundaram, E. Society, E. Society, and E. Society, Eds., *Silicon nitride and silicon dioxide thin insulating films: proceedings of the sixth international symposium*. Pennington: Electrochemical Society, 2001.
- [23] J. W. Goodman, *Introduction to Fourier optics*. New York: McGraw-Hill, 1988.
- [24] S. A. Self, “Focusing of spherical Gaussian beams,” *Applied Optics*, vol. 22, no. 5, p. 658, 1983.
- [25] L. D. Dickson, “Characteristics of a Propagating Gaussian Beam,” *Applied Optics*, vol. 9, no. 8, p. 1854, 1970.
- [26] R. M. Herman, J. Pardo, and T. A. Wiggins, “Diffraction and focusing of Gaussian beams,” *Applied Optics*, vol. 24, no. 9, p. 1346, 1985.
- [27] O. V. Minin and I. V. Minin, *Diffractive optics of millimetre waves*. Bristol, UK: Institute of Physics, 2004.
- [28] A. Siemion, “Terahertz Diffractive Optics—Smart Control over Radiation,” *Journal of Infrared, Millimeter, and Terahertz Waves*, vol. 40, no. 5, pp. 477–499, 2019.
- [29] G. J. Swanson and W. B. Veldkamp, “Diffractive Optical Elements For Use In Infrared Systems,” *Optical Engineering*, vol. 28, no. 6, 1989.

- [30] A. Arbabi, Y. Horie, A. J. Ball, M. Bagheri, and A. Faraon, “Subwavelength-thick lenses with high numerical apertures and large efficiency based on high-contrast transmitarrays,” *Nature Communications*, vol. 6, no. 1, p. 7069, 2015.
- [31] J. M. Nowosielski, R. Buczynski, F. Hudelist, A. J. Waddie, and M. R. Taghizadeh, “Nanostructured GRIN microlenses for Gaussian beam focusing,” *Optics Communications*, vol. 283, no. 9, pp. 1938–1944, 2010.
- [32] J. Nowosielski, R. Buczynski, A. J. Waddie, A. Filipkowski, D. Pysz, A. McCarthy, R. Stepien, and M. R. Taghizadeh, “Large diameter nanostructured gradient index lens,” *Optics Express*, vol. 20, no. 11, p. 11767, 2012.
- [33] A. I. Hernandez-Serrano, M. Weidenbach, S. F. Busch, M. Koch, and E. Castro-Camus, “Fabrication of gradient-refractive-index lenses for terahertz applications by three-dimensional printing,” *Journal of the Optical Society of America B*, vol. 33, no. 5, p. 928, 2016.
- [34] T. Søndergaard, M. O. Sauer, C. E. M. Nielsen, L. Merring-Mikkelsen, C. B. Sørensen, and E. Skovsen, “Theoretical analysis of compact cylindrical microlenses for terahertz photoconductive antennas in the photomixer regime,” *Journal of the Optical Society of America B*, vol. 37, no. 4, p. 1109, 2020.
- [35] Y. Arai, Y. Katano, K. Tsubaki, S. Uchida, and K. Kinoshita, “Silicon-germanium alloy for infrared GRIN materials,” in *Advanced Optics for Imaging Applications: UV through LWIR VI*, Online Only, 2021, p. 14.
- [36] N. Li, Z. Xu, Y. Dong, T. Hu, Q. Zhong, Y. H. Fu, S. Zhu, and N. Singh, “Large-area metasurface on CMOS-compatible fabrication platform: driving flat optics from lab to fab,” *Nanophotonics*, vol. 9, no. 10, pp. 3071–3087, 2020.
- [37] Y.-Y. Xie, P.-N. Ni, Q.-H. Wang, Q. Kan, G. Briere, P.-P. Chen, Z.-Z. Zhao, A. Delga, H.-R. Ren, H.-D. Chen, C. Xu, and P. Genevet, “Metasurface-integrated vertical cavity surface-emitting lasers for programmable directional lasing emissions,” *Nature Nanotechnology*, vol. 15, no. 2, pp. 125–130, 2020.
- [38] D. T. Pierce and W. E. Spicer, “Electronic Structure of Amorphous Si from Photoemission and Optical Studies,” *Physical Review B*, vol. 5, no. 8, pp. 3017–3029, 1972.
- [39] T. E. Sale, *Vertical cavity surface emitting lasers*. New York: Wiley, 1995.
- [40] P. Virtanen, R. Gommers, T. E. Oliphant, M. Haberland, T. Reddy, D. Cournapeau, E. Burovski, P. Peterson, W. Weckesser, J. Bright, S. J. van der Walt, M. Brett, J. Wilson, K. J. Millman, N. Mayorov, A. R. J. Nelson, E. Jones, R. Kern, E. Larson, C. J. Carey, Polat, Y. Feng, E. W. Moore, J. VanderPlas, D. Laxalde, J. Perktold, R. Cimrman, I. Henriksen, E. A. Quintero, C. R. Harris, A. M. Archibald, A. H. Ribeiro, F. Pedregosa, P. van Mulbregt, SciPy 1.0 Contributors, A. Vijaykumar, A. P. Bardelli, A. Rothberg, A. Hilboll, A. Kloeckner, A. Scopatz, A. Lee, A. Rokem, C. N. Woods, C. Fulton, C. Masson, C. Häggström, C. Fitzgerald, D. A. Nicholson, D. R. Hagen, D. V. Pasechnik, E. Olivetti, E. Martin, E. Wieser, F. Silva, F. Lenders, F. Wilhelm, G. Young, G. A. Price, G.-L. Ingold, G. E. Allen, G. R. Lee, H. Audren, I. Probst, J. P. Dietrich, J. Silterra, J. T. Webber, J. Slavić, J. Nothman, J. Buchner, J. Kulick, J. L. Schönberger, J. V. de Miranda Cardoso, J. Reimer, J. Harrington, J. L. C. Rodríguez, J. Nunez-Iglesias, J. Kuczynski, K. Tritz, M. Thoma, M. Newville, M. Kümmeler, M. Bolingbroke, M. Tartre, M. Pak, N. J. Smith, N. Nowaczyk, N. Shebanov, O. Pavlyk, P. A. Brodtkorb,

- P. Lee, R. T. McGibbon, R. Feldbauer, S. Lewis, S. Tygier, S. Sievert, S. Vigna, S. Peterson, S. More, T. Pudlik, T. Oshima, T. J. Pingel, T. P. Robitaille, T. Spura, T. R. Jones, T. Cera, T. Leslie, T. Zito, T. Krauss, U. Upadhyay, Y. O. Halchenko, and Y. Vázquez-Baeza, “SciPy 1.0: fundamental algorithms for scientific computing in Python,” *Nature Methods*, vol. 17, no. 3, pp. 261–272, 2020.
- [41] C. Deng, H. Kim, and H. Ki, “Fabrication of a compound infrared microlens array with ultrashort focal length using femtosecond laser-assisted wet etching and dual-beam pulsed laser deposition,” *Optics Express*, vol. 27, no. 20, p. 28679, 2019.
 - [42] W. L. Chan, H.-T. Chen, A. J. Taylor, I. Brener, M. J. Cich, and D. M. Mittleman, “A spatial light modulator for terahertz beams,” *Applied Physics Letters*, vol. 94, no. 21, p. 213511, 2009.
 - [43] A. Karvounis, B. Gholipour, K. F. MacDonald, and N. I. Zheludev, “All-dielectric phase-change reconfigurable metasurface,” *Applied Physics Letters*, vol. 109, no. 5, p. 051103, 2016.
 - [44] A.-K. U. Michel, D. N. Chigrin, T. W. W. Maß, K. Schönauer, M. Salinga, M. Wuttig, and T. Taubner, “Using Low-Loss Phase-Change Materials for Mid-Infrared Antenna Resonance Tuning,” *Nano Letters*, vol. 13, no. 8, pp. 3470–3475, 2013.
 - [45] J. Park, B. G. Jeong, S. I. Kim, D. Lee, J. Kim, C. Shin, C. B. Lee, T. Otsuka, J. Kyoung, S. Kim, K.-Y. Yang, Y.-Y. Park, J. Lee, I. Hwang, J. Jang, S. H. Song, M. L. Brongersma, K. Ha, S.-W. Hwang, H. Choo, and B. L. Choi, “All-solid-state spatial light modulator with independent phase and amplitude control for three-dimensional LiDAR applications,” *Nature Nanotechnology*, vol. 16, no. 1, pp. 69–76, 2021.